FORWARD MODELING THE GRAVITATIONAL FIELD USING A DIRECT SOLUTION OF POISSON'S EQUATION

by

Lauren E. Howell

A thesis submitted to the Faculty and the Board of Trustees of the Colorado School of Mines in partial fulfillment of the requirements for the degree of Master of Science (Mathematical and Computer Sciences).

Golden, Colorado

Date _____

Signed: _____
Lauren E. Howell

Signed: _____
Dr. Jon M. Collis
Thesis Advisor

Signed: _____
Dr. Yaoguo Li
Thesis Advisor

Golden, Colorado

Date _____

Signed: _____
Dr. Willy Hereman
Professor and Head
Department of Applied Mathematics and Statistics

ABSTRACT

Forward modeling of gravity data typically computes the vertical gravitational acceleration using either closed-form formulae, or numerical solution of Poisson's equation governing the gravity potential followed by numerical differentiation. We present a method for computing the vertical gravity anomaly directly from Poisson's equation governing the gravitational acceleration, formally relating the gravity anomaly to spatial derivatives of the density function. We first use a finite-difference approximation to obtain the numerical solution, which we later compare to a finite-volume solution approximation. The accuracy of this method is demonstrated through applications to synthetic models and comparisons with integral solutions. This method can also be easily adapted to compute the horizontal components of gravity anomaly with the same order of accuracy, thereby paving the way for studying the prospect of instrument development that may allow acquisition of the horizontal gravity components in the future.

TABLE OF CONTENTS

LIST OF FIGURES

LIST OF SYMBOLS

universal gravitational constant . . . . . γ

density . . . . . ρ

gravitational potential . . . . . ϕ

gravitational acceleration . . . . . $\mathbf{g}$

vertical component of gravitational acceleration . . . . . g_z

horizontal (x dimension) component of gravitational acceleration . . . . . g_x

horizontal (y dimension) component of gravitational acceleration . . . . . g_y

ACKNOWLEDGMENTS

I would like to express my deepest gratitude to Asst. Professor Collis and Assoc. Professor Li, my research advisors, for their patient guidance, supportive encouragement, and useful critiques of my thesis work. I cannot say enough to thank them for their tremendous help and inspiration. I would also like to thank the members of my thesis committee, Professors Ganesh and Martin, without whose knowledge and assistance this study would not have been successful. Special thanks to Anya Reitz, Cici Martinez, Leon Foks, and all the other members of CGEM for generously sharing their time and ideas. My thanks and appreciation also go out to my fellow graduate students Kimberly Spencer, Greg Johnson, Joey Maestas, Eric Threet, Brennan Sprinkle, and Jackie Henderson. They shared their knowledge, ideas, and numerous tips, all of which culminated in the successful completion of this project. Finally, I would like to express my love and heartfelt thanks to my family for their patience, encouragement, and constant support throughout this, and all of my endeavours.

To my parents, Sue and Wayne,

and my sister, Katy,

for always being there.

CHAPTER 1

INTRODUCTION

Borehole gravity surveys have been shown to detect information about features in the subsurface with more details than surface gravity surveys. The improved resolution of subtle changes in density has important applications for 4D reservoir monitoring and characterization of complex 3D structures. The 4D gravity method may provide a inexpensive means of reservoir management as a supplement to traditional 4D seismic surveys. Furthermore, the latest borehole gravimeters are capable of acquiring data in highly deviated (60° off vertical) or even horizontal wells [1]. These new developments open the avenue for novel reservoir monitoring methods with a broad range of possible well placement. Therefore, it is important to have the corresponding modeling techniques that can rapidly simulate gravity anomalies at arbitrary observation locations in 3D space due to complex reservoirs and associated density changes.

Traditional modeling approaches that use a volume integral representation of the gravity field may suffer from singularities, which arise when numerical computation points lie inside or on the boundary of the source body. Attempts to avoid these singularities impose restrictions on the location of the observation points relative to the source body. A review is provided by [2]. These methods can be computationally inefficient for large data sets with complex density distributions. More recently, numerical methods have been used to simulate the gravitational field by computing the components of gravitational acceleration from potential obtained through the solution of Poisson's equation. These techniques are more efficient than the integral form solution in that they reduce computation time and memory usage, and hence are useful for forward modeling of large data sets and for certain inversion procedures.

We introduce a numerical solution to Poisson's equation that directly solves for scalar components of the gravitational field. This approach enjoys the same benefits in computation time and memory usage as other numerical solutions of Poisson's equation for gravitational potential. In this paper, we consider traditional solutions as well as our direct numerical method, and demonstrate finite-difference and finite-volume formulations for solving Poisson's equation for components of the gravitational field, first using synthetic examples and then applying the method to a realistic data set.

CHAPTER 2

BACKGROUND

This chapter details the requisite knowledge related to simulating the gravitational field, including conventional solution techniques and their appropriate areas of application. First, relevant concepts from potential theory are outlined, followed by a discussion of common features of gravity studies, making special emphasis of borehole gravity surveys. Finally, two classical forward modeling techniques are highlighted, noting the limitations and benefits of each one. This leads into an introduction of our new numerical partial differential equation solution.

2.1 Potential theory

Newton's law of universal gravitation describes the mutual attractive force between two point masses; the magnitude of this force is directly proportional to the product of the masses and inversely proportional to the square of the distance between them. In Cartesian coordinates, $\mathbf{F}$ describes the mutual force between two point masses, m at $Q = (x', y', z')$ and m_0 at $P = (x, y, z)$,

$$\mathbf{F} = \gamma \frac{m m_0}{r^2}, \tag{2.1}$$

where γ is the universal gravitational constant and

$$r = \sqrt{(x - x')^2 + (y - y')^2 + (z - z')^2}$$

is the distance between the two masses.

To describe the gravitational attraction produced by one mass at the location of the other, we treat m_0 as a test particle with unit mass, and obtain $\mathbf{g}$, the *gravitational attraction* produced by mass m at point P:

$$\mathbf{g}(P) = -\gamma \frac{m}{r^2} \hat{\mathbf{r}}, \tag{2.2}$$

where the unit vector directed from the mass m to the location P, in Cartesian coordinates, is

$$\hat{\mathbf{r}} = \frac{1}{r}\Big[(x-x')\hat{\mathbf{i}} + (y-y')\hat{\mathbf{j}} + (z-z')\hat{\mathbf{k}}\Big].$$

The minus sign in Equation 2.2 appears due to the convention that $\hat{\mathbf{r}}$ points away from the source toward the observation point. Using Equation 2.1, the force acting upon the smaller body is described by $\mathbf{F} = m_0\mathbf{g}$. Hence, we notice that $\mathbf{g}$ has units of acceleration, leading to its equivalent description, *gravitational acceleration*. Gravitational acceleration is a conservative force, and can be represented as the gradient of a scalar potential ϕ, called *gravitational potential*:

$$\mathbf{g}(P) = \nabla\phi(P), \tag{2.3}$$

where

$$\phi(P) = \gamma\frac{m}{r}.$$

2.1.1 Considering distributions of mass

The superposition principle can be applied to determine the gravitational attraction of a continuous distribution of matter, which is defined as a collection of very small masses $\delta m = \rho(x,y,z)\mathrm{dv}$, where $\rho(x,y,z)$ is the density distribution. Integrating over the volume of the body, the contribution to potential from each small element δm can be calculated. Hence,

$$\phi(P) = \gamma\int_V \frac{\delta m}{r} = \gamma\int_V \frac{\rho(Q)}{r}\mathrm{dv}, \tag{2.4}$$

where P is the point of observation, Q is the point of integration within the mass, and r is the distance between P and Q. Integration is over the volume of the entire mass, V. To obtain Poisson's equation for gravitational potential, take the Laplacian of both sides of Equation 2.4, and by the result from [3, pg.23], we obtain

$$\nabla^2\phi(P) = -4\pi\gamma\rho(P). \tag{2.5}$$

Equation 2.5 is Poisson's equation for gravitational potential. It is valid at all points, both outside, where $\rho = 0$, and inside the mass distribution. It can be shown that outside the mass, Poisson's equation reduces to Laplace's equation [4]. It should be emphasized here that gravitational potential ϕ and gravitational acceleration $\mathbf{g}$ exist and are continuous throughout space if caused by a bounded distribution of piecewise-continuous density. In our work, we approximate continuous density distributions by piecewise-constant functions. Also, ϕ is everywhere differentiable, so the relation $\mathbf{g} = \nabla\phi$ from Equation 2.3 holds everywhere.

2.1.2 Units

Using the SI unit for gravitational acceleration, the value of gravity at the Earth's surface is approximately 9.81 m·sec^{-2}. This unit is unpractical for use in geophysics, where the cgs system is preferred. In cgs units, mass is in grams, distance is in centimeters, and gravitational acceleration is in cm·sec^{-2}. Here, the unit of acceleration is often referred to as Gal, where 1 Gal = 1 cm·sec^{-2}. In geophysical literature, gravitational attraction is often reported in units of mGal, (1 mGal = 10^{-3} Gal). Modern instruments are capable of measuring gravity variations to a millionth of a gal, or microgal (μGal).

The universal gravitational constant is reported as 6.67×10^{-11} m^3·kg^{-1}·sec^{-2} in SI units, and 6.67×10^{-8} cm^3·g^{-1}·sec^{-2} in cgs units. Density ρ has units kg·m^{-3} in the SI, and g·cm^{-3} in cgs units. Conversion between the SI and cgs systems is accomplished using the relation 1 kg·m^{-3} = 10^{-3} g·cm^{-3}. Following the geophysical convention, cgs units are used exclusively.

2.2 The gravity method

Geophysicists use gravity measurements as an indirect way of describing the irregular distribution of subsurface structures. For example, gravity data can help describe the structure of continental margins and sedimentary basins, locate salt structures and high-density ore bodies for oil and mineral exploration, and monitor fluid movement in reservoirs, [5–8]. Gravity surveys are relatively cheap, and can cover large areas while still maintaining a high degree of accuracy in the measurements.

Instruments called gravimeters measure variations in gravitational acceleration—frequently, the vertical component—arising from the density distribution of the Earth's subsurface. Gravimeters have been developed for a variety of data aquisition scenarios. Beginning with land-based operations, developments in instrumentation now accomodate marine, submarine, ocean-bottom, airborne, and borehole gravity surveys. Borehole surveys have been shown to detect information about features in the subsurface in more detail than airborne or surface gravity surveys. The improved resolution of subtle changes in density has important applications for 4D reservoir monitoring and the characterization of complex 3D structures. However, unlike other data aquisition methods, borehole gravity surveys measure gravity variations from within the subsurface, gathering data inside a borehole. This poses challenges for computing solutions using traditional methods.

There are three components of gravitational acceleration, two horizontal components (g_x, g_y), and a vertical component (g_z):

$$\mathbf{g} = \begin{pmatrix} g_x \\ g_y \\ g_z \end{pmatrix}.$$

The vertical component is defined as perpendicular to the equipotential surface, while the plane tangential to the equipotential surface defines the horizontal components. Of the three, the vertical component is of greatest interest in geophysics, although instrumentation capable of measuring the horizontal components is on the horizon. The measurements are plotted, forming profiles of gravity data over the causative region. A series of corrections to these data are usually performed, yielding gravity anomaly plots that are used to isolate and interpret subsurface features of interest. More information about these corrections, and the gravity method in general, can be found in references [7] and [9].

After processing, the data are used to construct a model of subsurface density distribution through inversion. To further constrain the result, the inversion scheme may also include information independent of the measured data, if available. Successful inversion schemes require accurate and efficient forward models that compute the gravity field arising from a

known density distribution. It is important to note that different density distributions can result in identical gravity anomalies. This non-uniqueness poses a fundamental challenge in interpreting gravity anomalies.

It is important to note that geophysical discussions of gravity anomalies often refer to density contrast, rather than simply density. Because the purpose of these studies is to isolate particular regions in the subsurface, the density of the body of interest is taken in contrast to the density of the surrounding, background material. Density contrast defines the difference between the density of the source body and the background; hence, in density contrast terms, the background density is zero. Because we consider only forward models in our study—where we define the source and background densities of the region—we do not make this distinction between density and density contrast. Formulating solutions in terms of density contrast is appropriate for inverse problems, where the density distribution in the subsurface is initially unknown.

2.3 Traditional solution methods

Forward models of gravity data have historically used closed-form, analytic solutions of integrals to compute vertical gravity anomalies. This approach is well-established in the geophysical community, and while it is effective for small-scale problems, it has a few drawbacks in practical applications. This approach uses a volume integral representation of the gravity field; analytical solutions of this volume integral may suffer from singularities. Attempts to avoid these singularities imposes restrictions on the location of the observation points relative to the source body. Modern applications of this method have demonstrated that its main drawback arises in computing the analytic solutions numerically. Compared to newer methods that compute solutions of the vertical gravitational acceleration from Poisson's equation for gravitational potential, the integral solution approach can be computationally inefficient, particularly when using large data sets associated with complex density distributions.

In response to these limitations, numerical methods that model the gravity field by computing the components of gravitational potential obtained through the solution of Poisson's

equation have been developed. It has been shown [10–12] that these techniques produce accurate solutions that benefit from reduced computation time and memory usage. In addition, some of these methods can easily accomodate modeling using unstructured grids, which allows sources with complex geometry to be modeled more accurately and efficiently than with regular grids [12]. These newer methods represent the current thrust of research in the development of three-dimensional gravity forward modeling techniques.

2.3.1 Integral form

The gravitational attraction $\mathbf{g}$ at a point $P = (x, y, z)$ due to a volume V can be expressed in an integral form by

$$\mathbf{g}(P) = -\gamma \int_V \rho \frac{\hat{\mathbf{r}}}{r^2} dv, \tag{2.6}$$

where ρ is density as a function of space, r is the distance from the observation point P to an element of the body dv, $\hat{\mathbf{r}}$ is a unit vector pointing from an element of the mass to P, and γ is the universal gravitational constant [4]. We integrate over the region V that constitutes our model space, and use a Cartesian coordinate system where the z-axis is taken to be pointing vertically down. Note that this formula is valid in the whole space, however, in practice, an analytic solution must be derived in order to build geologic models.

Gravimeters typically measure the vertical attraction of gravity, in the z direction under our coordinate system. There are a variety of equivalent expressions for this quantity, denoted here by g_z. One that is commonly used in geophysical applications is obtained by considering the z component of Equation 2.6; it computes the vertical gravitational attraction of a mass distribution with density $\rho(x', y', z')$ observed at point (x, y, z),

$$g_z = -\gamma \int_{z'} \int_{y'} \int_{x'} \rho(x', y', z') \frac{(z - z')}{r^3} \mathrm{d}x' \mathrm{d}y' \mathrm{d}z'. \tag{2.7}$$

Forward modeling studies of gravity data have historically used this integral to solve for the vertical component of the gravity field. There are a number of closed-form solutions to Equation 2.7 that are typically used to compute an exact result for the gravitational

attraction of a given 3D source body. Popular categories of the geometric structures used to model source bodies are the stack of right rectangular prisms, the stack of polygonal prisms, and the polyhedron; each of these models use different analytical formulas to compute solutions. The choice of model for a given problem is motivated by a variety of factors such as the source geometry, how much additional geologic information is known about the region, the type of gravity survey conducted, the desired efficiency and accuracy of computation, and so on. As one might expect, the contributions from these factors can either reduce or augment the challenges in computing a solution to a given problem; proper care must be taken in weighing the relative contribution of each of these factors against one another.

It is important to note that these analytical formulas have singularities for observation points located on the facets or edges of the body and can fail in numerical implementations. This is problematic for borehole gravity surveys, as the observations points are located within the subsurface and may coincide with facets or edges of the discretized density representation. Furthermore, this approach is inefficient for surveys with a large number of observation points, as computation time depends on the number of observations [12]. The analytical formula approach also requires the use of a matrix that describes the geometry between the source and the observation points during the inversion. This matrix is dense, making it expensive to store, and presents particular difficulty when inverting large data sets [11]. For geophysical applications, the rapid simulation of gravity anomalies in 3D space is of great interest, but the complex source geometry involved in these types of problems presents challenges to the efficiency of computing numerical solutions to the integral.

In geophysical literature, Equation 2.7 is often referred to as an *integral equation*. Indeed, for inverse problems, where ρ is unknown and g_z is known, Equation 2.7 is a Fredholm integral equation of the first kind. However, for forward modeling applications such as those explored here, Equation 2.7 is not a true integral equation, since ρ is known and g_z is unknown. Hence, we refer to Equation 2.7 as an integral solution or integral form; elsewhere in the literature, this or similar expressions may be called integral equations.

2.3.2 Numerical differentiation

Methods involving the numerical solution of Poisson's equation have been used as alternatives to the integral solution approach. These approaches obtain numerical solutions to Equation 2.5 and then compute the vertical component of the gravity field by making use of the relation given in Equation 2.3, typically using standard discrete approximations. In their forward models, Zhang et al., [13], use a finite-element solution to Poisson's equation, Mosher et al., [10], employ a finite-difference approach, and Farquharson and Mosher, [11], compute solutions using the finite-volume method. In computing the numerical solution to Poisson's equation, these methods generally discretize the domain using a rectangular grid, forming a mesh where the density in each cell is assumed to be constant. If the cells are sufficiently small, this type of mesh can be used to reproduce virtually any density distribution, and, due to its simplicity, implementation of numerical algorithms is straightforward. Irregular grids increase the complexity of the scheme, but also increase the capability of modeling complex structures using fewer cells than regular grids [12]. Once the region is discretized, gravitational potential within each cell is approximated by a numerical solution of Poisson's equation. Finite-difference solutions are well-established, while finite-element and finite-volume methods also result in robust schemes.

Numerical methods have been shown to have benefits over closed-form solutions in a few key areas. An advantage to the aforementioned methods is that they do not deteriorate due to singularities in the solution. Also, the finite-volume solution in reference [11] requires less memory than other programs used to invert dense matrices. Finally, for studies involving large data sets, computation time of the finite-volume method for unstructured grids is lower than for the closed-form solution method [12].

Throughout this paper we refer to this approach as the *numerical differentiation* solution. This is due to the derivative approximation that is used to obtain g_z—via Equation 2.3—from the gravitational potential solution to Equation 2.5. With this choice of nomenclature, our intent is to highlight the difference between this particular numerical solution and our

newly developed numerical solution (the *direct* solution), which does not require numerical differentiation.

2.4 Current work: Direct solution

We present a numerical partial differential equation solution for the gravitational field, in which we solve directly for a component of the gravity field. For example, for the vertical component, Equation 2.3 gives $g_z = \partial\phi/\partial z$ in Equation 2.5, yielding our new formulation

$$\nabla^2 g_z = -4\pi\gamma \frac{\partial \rho}{\partial z}. \tag{2.8}$$

We solve this equation for g_z numerically, using finite-difference and finite-volume formulations, given a density distribution ρ (note that $\rho = 0$ outside the source volume). This process can be repeated for the horizontal components (g_x, g_y) of the gravity field. This solution inherently avoids the types of singularities that arise in the integral solution. This is because we do not distinguish between observation and evaluation points under this approach. Here, the gravitational field is calculated everywhere in the domain, rather than pointwise at specific observation locations. Consequently, the dense matrix used in the integal solution to describe the geometry between the source and observation points does not arise in the direct solution. Instead, the direct solution results in a linear system with a sparse matrix, giving it the same benefits in computation time and memory usage as the numerical differentiation solution.

We refer to this solution as the *direct* solution because it computes components of the gravity field directly. The gravity field decays more rapidly (inverse distance squared) than the potential itself (inverse distance), so the direct solution will require a smaller mesh in order to approximate the boundary conditions to the same degree as would be required for the solution of gravitational potential. Avoiding the step of numerical differentiation of the gravitational potential will also maintain the order of accuracy of the solution.

2.4.1 Density derivative function

Recall that the numerical differentiation solution uses Poisson's equation to compute gravitational potential. In this case, the solution of the governing equation (potential) must be differentiated to obtain the desired vertical gravity solution. The formulation of Poisson's equation given in Equation 2.8 allows the vertical component of gravitational acceleration to be computed directly—that is, solving the governing equation results immediately in g_z. The direct result is achieved by differentiating the right-hand side density distribution function, rather than gravitational potential as in the numerical differentiation solution. The density derivative is a key feature of this approach; it results in a direct solution of gravitational acceleration, but it introduces mathematical challenges that do not arise in other methods.

In the physical world, density varies continuously in the subsurface. To approximate the gravity field arising from such density distributions, numerical models discretize the region using regular or irregular meshes, where each cell is assumed to have uniform density. That is, density is defined as a piecewise constant function in the domain. Unlike traditional numerical solutions, the direct method requires taking a derivative of this function. Hence, within each cell (where density is known) the derivative exists, but on the boundaries between cells the derivative is not defined in the classical sense. To alleviate this issue mathematically, weak derivative treatments of the density derivative function are considered, allowing numerical solutions to be computed for these types of problems.

Initially, the direct solution is computed using a finite-difference scheme. Even though $\partial\rho/\partial z$ may be a non-continuous function, the governing equation is only evaluated on the continuous segments that lie within each cell. We do not evaluate solutions on the boundaries of each cell, where the singularities in the density distribution function lie. Note that $\partial\rho/\partial z$ is mostly zero throughout the domain, however near a density discontinuity—such as a source edge—the finite-difference approximation yields a nonzero value.

A finite-volume scheme is implemented to alleviate the problems associated with the density derivative function. Under this approach, the governing equation Equation 2.8 is

integrated over each cell volume; using the fundamental theorem of calculus we are able to replace the density derivative from the right-hand side of Equation 2.8 with an equivalent representation using the original density distribution function ρ. By evaluating the density derivative analytically, we avoid the numerical derivative approximation used in the numerical differentiation solution.

2.4.2 Boundary conditions

In mathematical modeling, three types of boundary conditions are typically encountered: Dirichlet, Neumann, and Robin (or mixed) conditions. For geophysical applications, a Robin (or mixed) boundary condition is preferable. With homogenous Dirichlet conditions, the domain is taken to be large enough so that the field decays to zero everywhere on the boundary. For example, gravitational potential decays like $1/r$, where r is the distance between the observation point and the causative mass. Gravitational acceleration decays more rapidly, behaving like $1/r^2$. Homogenous Neumann conditions may also be used, and are defined anywhere where a normal derivative exists on the boundary—a condition that is problematic when consider corners of a rectangular domain. Dey and Morrison, [14], find that the Dirichlet condition tends to undershoot the calculated field, while the Neumann condition tends to overshoot the field. They propose that a Robin boundary condition yields a better fit between the numerical and analytical solution values, while removing the need for an a priori assumption about the nature of the field along the boundaries.

For our problem, we use the Robin boundary condition

$$\alpha g_z + \frac{\partial g_z}{\partial n} = 0, \tag{2.9}$$

where α is a parameter with cgs units cm^{-1}. The boundary condition enters the problem in the matrix of the linear system used to approximate the numerical solution to Equation 2.8; it is used to define values in the matrix at points near the boundaries. In our work, we make the approximation $\alpha = 1$; a more precise treatment of this parameter can be found in [14], where they determine the value of α at each point on the boundary.

2.4.3 Linear system

Both the finite-difference and finite-volume formulations of the direct solution result in a linear system of the form $\mathbf{Ax} = \mathbf{b}$. Here, $\mathbf{A}$ is a sparse banded matrix that connects elements of the system with one another, $\mathbf{x}$ is the gravitational acceleration solution approximation vector, and $\mathbf{b}$ is a vector containing information about the density distribution of the model. The structure of the stiffness matrix $\mathbf{A}$ is the same for both the finite-difference and finite-volume solutions, although the values along the nonzero diagonals differ due to the difference in grid construction between the schemes. The load vector $\mathbf{b}$ is composed of mostly zero values (since the density values in the domain are mostly zero), but has nonzero entries near the edges of the source. In the finite-difference scheme these values arise from derivative approximations, while the finite-volume scheme computes the difference in density value between adjacent cells. In both cases, the load vector is populated by only a few nonzero values; care must be taken in the implementation of the scheme not to "miss" significant density information contained in these few entries.

2.5 Summary

We began this chapter with a description of concepts from potential theory and discussed how they are relevant in the types of problems we consider here. Two key expressions we introduced were Equations 2.3 and 2.5; the first relates gravitational acceleration and gravitational potential, and the second relates a density distribution to the resultant field of gravitational potential. Then, we highlighted some key features of the gravity method, including a discussion on the differences between borehole gravity surveys and other survey approaches. Next we outlined features of two traditional techniques for computing gravitational acceleration: the integral and numerical differentiation solutions. Finally, we present our newly developed direct solution for components of gravitational acceleration (Equation 2.8), and describe characteristics of implementing this solution numerically. Next, we give a more detailed description of the numerical schemes used to compute the direct solution.

CHAPTER 3

FINITE-DIFFERENCE SCHEME

For a given density distribution representing a subsurface region of the Earth, we construct a forward model based on Equation 2.8 that is used to compute the resulting gravity anomaly. In our study, we treat gravitational acceleration as a Laplacian field and solve directly for the component of interest. Given that the finite-difference method is a well established numerical solution technique, we consider it an appropriate starting place for solving problems of this type. We begin by discussing the motivation for our choice of boundary conditions. We then describe our finite-difference scheme in two and three dimensions. This description involves a discussion on the construction of the matrix-vector form of the scheme.

3.1 Boundary conditions

The value of the gravitational field must be specified along the edges of the computational domain Ω, which are located "infinitely" distant from the source body; that is, the grid is extended far enough away from the source such that the calculated field behaves asymptotically. The field values at the boundaries of the domain can be specified with a priori information about the gravitational flux, although, in real applications these values cannot be computed analytically [14]. In such cases, a Dirichlet or Neumann condition is assumed. Dey and Morrison, [14] assert that a Robin boundary condition is the best choice for geophysical problems such as the ones considered here. However, in real applications, this formulation is equivalent to a zero Dirichlet boundary condition [15]. We have verified this conclusion on a two-dimensional test problem, and thus proceed with a zero Dirichlet condition in our three-dimensional scheme.

3.2 Two dimensional scheme

We begin by deriving the numerical solution method for computing vertical gravity in two dimensions—the extension to three dimensions will be discussed later. On a typical two dimensional Cartesian grid, let z be the vertical axis (positive down) and x be the horizontal axis. We choose z here instead of the traditional y to maintain the geophysical convention of depth being described in terms of the z component. Let us consider a rectangular computational domain $\Omega = \{(x, z) \in \mathbb{R}^2 : a_x \leq x \leq b_x,\ a_z \leq z \leq b_z\}$ where a_x, b_x, a_z, b_z are real numbers.

Simplifying notation, we call our solution $g_z = u(x, z)$, which satisfies

$$\nabla^2 u(x, z) = -af(x, z), \tag{3.1}$$

where $a = 4\pi\gamma$ and

$$f(x, z) = \frac{\partial \rho(x, z)}{\partial z}.$$

Note that most of the computational domain will have zero density, with some positive density value only within the source itself. Based on the results described in the previous section, we implement zero Dirichlet boundary conditions on the domain:

$$u(a_x, z) = u(b_x, z) = u(x, a_z) = u(x, b_z) = 0, \quad \text{for all } x, z \in \partial\Omega.$$

We also have a two-dimensional body of interest located within the domain, referred to as the source. The method requires that the source be much smaller than the domain itself. This means that in Ω most values will be zero, but the source will generate a small region of positive values. In our initial development of the forward model, we take as a source a small square with a density of 1 g/cm^3, located at the center of the computational domain. Later, the source is defined using geophysical field data.

Let M and N be positive integers, putting

$$h_x = \frac{b_x - a_x}{M}, \quad h_z = \frac{b_z - a_z}{N}.$$

Hence, $x_m = mh_x$ and $z_n = nh_z$ are grid points on the x and z axes, respectively. This gives

$$U_{mn} \approx u(x_m, z_n), \quad f_{mn} \approx f(x_m, z_n), \quad \text{for } 0 \leq m \leq M \text{ and } 0 \leq n \leq N.$$

We approximate the Laplacian using second derivative approximations δ_x^2 and δ_z^2 on Equation 3.1, yielding the discrete Laplacian

$$\nabla_h^2 U_{mn} = \delta_x^2(U_{mn}) + \delta_z^2(U_{mn}) = \frac{U_{m+1n} - 2U_{mn} + U_{m-1n}}{h_x^2} + \frac{U_{mn+1} - 2U_{mn} + U_{mn-1}}{h_z^2}. \quad (3.2)$$

Here, we maintain the geophysical convention of notating the Laplacian using ∇^2. Hence, the finite difference method for Equation 3.1 is

$$\nabla_h^2 U_{mn} = -af_{mn} \quad \text{for } 1 \leq m \leq M-1,\ 1 \leq n \leq N-1 \quad (3.3)$$

with boundary conditions

$$U_{0n} = U_{Mn} = U_{m0} = U_{mN} = 0, \quad \text{for } 1 \leq m \leq M-1,\ 1 \leq n \leq N-1.$$

3.2.1 Matrix-vector form

To construct the matrix-vector form of this method, notice that Equation 3.3 represents a $(M-1)(N-1) \times (M-1)(N-1)$ dimensional system. Let

$$\mathbf{u}_m = [U_{m1} \dots U_{mN-1}]^T, \quad \text{and} \quad \mathbf{f}_m = [f_{m1} \dots f_{mN-1}]^T$$

be $N-1$ dimensional vectors for fixed $1 \leq m \leq M-1$. Then we construct solution vector $\mathbf{U}$ and load vector $\mathbf{F}$ by stacking $\mathbf{u}_m$ and $\mathbf{f}_m$ for $1 \leq m \leq M-1$:

$$\mathbf{U} = [\mathbf{u}_1 \dots \mathbf{u}_{M-1}]^T, \quad \text{and} \quad \mathbf{F} = [\mathbf{f}_1 \dots \mathbf{f}_{M-1}]^T. \quad (3.4)$$

By writing Equation 3.3 as a system of equations in the usual way, it is clear that it can be expressed in matrix-vector form as $\mathbf{AU} = \mathbf{F}$, where $\mathbf{A}$ is a $(M-1)(N-1) \times (M-1)(N-1)$ sparse finite difference matrix with 5 diagonals,

$$\mathbf{A} = \begin{bmatrix} \left(\mathbf{B} - \frac{2}{h_x^2}\mathbf{I}\right) & \frac{1}{h_x^2}\mathbf{I} & & 0 \\ \frac{1}{h_x^2}\mathbf{I} & \ddots & \ddots & \\ & \ddots & \ddots & \frac{1}{h_x^2}\mathbf{I} \\ 0 & & \frac{1}{h_x^2}\mathbf{I} & \left(\mathbf{B} - \frac{2}{h_x^2}\mathbf{I}\right) \end{bmatrix},$$

with

$$\mathbf{B} = -\frac{1}{h_z^2}\begin{bmatrix} 2 & -1 & & 0 \\ -1 & \ddots & \ddots & \\ & \ddots & \ddots & -1 \\ 0 & & -1 & 2 \end{bmatrix}$$

as the $(N-1)\times(M-1)$ dimensional matrix on the main diagonal, and $\mathbf{I}$ as the $(N-1)\times(M-1)$ dimensional identity matrix. We derive this result by considering the second derivative approximations of the $N-1$ dimensional vectors $\mathbf{u}_m$ and $\mathbf{f}_m$, and writing these as a system of $M-1$ vector equations. For example, take $\delta_z^2(\mathbf{u}_m)$ for $1 \leq m \leq M-1$:

$$\delta_z^2(\mathbf{u}_m) = \begin{bmatrix} U_{m0} - 2U_{m1} + U_{m2} \\ U_{m1} - 2U_{m2} + U_{m3} \\ \vdots \\ U_{mN-2} - 2U_{mN-1} + U_{mN} \end{bmatrix} = \mathbf{B}\mathbf{u}_m, \tag{3.5}$$

since we have zero boundary conditions—i.e. $U_{m0} = U_{mN} = 0$. Hence, using Equation 3.5 in Equation 3.3, we obtain $M-1$ vector equations,

$$\mathbf{B}\mathbf{u}_1 + \left(\frac{\mathbf{u}_0 - 2\mathbf{u}_1 + \mathbf{u}_2}{h_x^2}\right) = \mathbf{f}_1$$

through

$$\mathbf{B}\mathbf{u}_{M-1} + \left(\frac{\mathbf{u}_{M-2} - 2\mathbf{u}_{M-1} + \mathbf{u}_M}{h_x^2}\right) = \mathbf{f}_{M-1},$$

where $\mathbf{u}_0 = \mathbf{u}_M = \mathbf{0}$. This yields the system

$$\begin{bmatrix} \mathbf{B}\mathbf{u}_1 \\ \mathbf{B}\mathbf{u}_2 \\ \vdots \\ \mathbf{B}\mathbf{u}_{M-1} \end{bmatrix} + \frac{1}{h_x^2}\begin{bmatrix} -2\mathbf{u}_1 + \mathbf{u}_2 \\ \mathbf{u}_1 - 2\mathbf{u}_2 + \mathbf{u}_3 \\ \vdots \\ -2\mathbf{u}_{M-1} + \mathbf{u}_M \end{bmatrix} = \begin{bmatrix} \mathbf{f}_1 \\ \mathbf{f}_2 \\ \vdots \\ \mathbf{f}_{M-1} \end{bmatrix},$$

which can be expressed as $\mathbf{AU} = \mathbf{F}$.

The zero boundary conditions require that certain entries on the $1/h_z^2$ diagonals be zero; the location of these zero entries is determined by examining the overall structure of the

matrix, which can be thought of as a tridiagonal block matrix, where

$$\mathbf{D} = \left(\mathbf{B} - \frac{2}{h_x^2}\mathbf{I}\right) = \begin{bmatrix} \left(-\frac{2}{h_z^2} - \frac{2}{h_x^2}\right) & \frac{1}{h_z^2} & & 0 \\ \frac{1}{h_z^2} & \ddots & \ddots & \\ & \ddots & \ddots & \frac{1}{h_z^2} \\ 0 & & \frac{1}{h_z^2} & \left(-\frac{2}{h_z^2} - \frac{2}{h_x^2}\right) \end{bmatrix}$$

is the main diagonal block and

$$\mathbf{C} = \frac{1}{h_x^2}\mathbf{I} = \begin{bmatrix} \frac{1}{h_x^2} & & & 0 \\ & \ddots & & \\ & & \ddots & \\ 0 & & & \frac{1}{h_x^2} \end{bmatrix}$$

forms the sub- and super-diagonal blocks, with $\mathbf{I}$ as the $(N-1) \times (M-1)$ dimensional identity matrix. Hence,

$$\mathbf{A} = \begin{bmatrix} \mathbf{D} & \mathbf{C} & & \mathbf{0} \\ \mathbf{C} & \ddots & \ddots & \\ & \ddots & \ddots & \mathbf{C} \\ \mathbf{0} & & \mathbf{C} & \mathbf{D} \end{bmatrix},$$

where $\mathbf{0}$ is the zero matrix with dimensions $(N-1) \times (M-1)$. The zero entries lie between the ends of the sub- and super-diagonals (with entries $1/h_z^2$) of $\mathbf{D}$, between sequential $\mathbf{D}$ matrix blocks. This region is also defined by the lower left (for the super-diagonal in $\mathbf{D}$) and the upper right (for the sub-diagonal in $\mathbf{D}$) corners of the sub- and super-diagonal block matrix $\mathbf{C}$. In the three-dimensional problem, the matrix structure is similar, and can also be described using block matrices; this topic will be discussed later.

Recall that the entries of $\mathbf{F}$ are defined by

$$f_{mn} \approx f(x_m, z_n) = \frac{\partial \rho(x_m, z_n)}{\partial z}, \tag{3.6}$$

for $1 \leq m \leq M-1$ and $1 \leq n \leq N-1$. In order to obtain values f_{mn} to use in our linear system, we apply a central difference approximation to the derivative in Equation 3.6 as follows,

$$f_{mn} \approx \frac{\rho(x_m, z_{n+1}) - \rho(x_m, z_{n-1})}{2h_z}.$$

Even though ρ is a non-continuous function, the central difference approximation—and hence the derivative—is only evaluated on the continuous segments of the density function. In our numerical approximation, we assume constant density values within each cell of the grid; as such, these continuous segments are defined by each cell in the computational domain. Furthermore, if density values on the non-continuous points between each cell were desired, these values could be interpolated from the density values of the surrounding cells.

Therefore, in solving for the numerical solution of vertical gravity, U_{mn}, the vertical derivative of the density function over the entire domain is approximated using a central difference, and is then used in solving the linear system $\mathbf{AU} = \mathbf{F}$ for $1 \leq m \leq M-1$ and $1 \leq n \leq N$. This procedure can be easily modified to solve for the horizontal component of the gravity field by taking a central difference approximation of the density in x.

3.3 Three dimensional scheme

Here, we explore the additional elements of solving the three-dimensional version of Equation 3.1. The procedure is the same as for the two-dimensional case, with the most significant differences found in constructing the matrix-vector form of the scheme. We describe the structure of the linear system, leaving the reader to refer to the two-dimensional case as needed. In three dimensions, the computational domain is defined $\Omega = \{(x, y, z) \in \mathbb{R}^3 : a_x \leq x \leq b_x, a_y \leq y \leq b_y, a_z \leq z \leq b_z\}$ where $a_x, b_x, a_y, b_y, a_z, b_z$ are the physical dimensions of the computational domain. Letting L, M and N be positive integers, and defining grid spacing parameters as

$$h_x = \frac{b_x - a_x}{L}, \quad h_y = \frac{b_y - a_y}{M}, \quad h_z = \frac{b_z - a_z}{N}.$$

Hence, $x_\ell = \ell h_x$, $y_m = m h_y$ and $z_n = n h_z$ are grid points on the x and z axes, respectively, where $1 \leq \ell \leq L$, $1 \leq m \leq M$, $1 \leq n \leq N$. We define our gravitational acceleration and density contrast derivative values on the grid: $U_{lmn} \approx g_z(x_\ell, y_m, z_n)$, and $f_{lmn} \approx f(x_\ell, y_m, z_n)$,

where

$$f(x,y,z) = \frac{\partial \rho(x,y,z)}{\partial z},$$

for $0 \leq \ell \leq L$, $0 \leq m \leq M$, $0 \leq n \leq N$. The finite-difference method for Equation 2.8 is

$$\nabla^2 U_{\ell mn} = -4\pi\gamma f_{\ell mn}, \tag{3.7}$$

defined on the interior of the grid, i.e. for $1 \leq \ell \leq L-1$, $1 \leq m \leq M-1$, $1 \leq n \leq N-1$, where

$$\nabla^2 U_{\ell mn} = \frac{U_{\ell+1mn} - 2U_{\ell mn} + U_{\ell-1mn}}{h_x^2} + \frac{U_{\ell m+1n} - 2U_{\ell mn} + U_{\ell-1mn}}{h_y^2} + \frac{U_{\ell mn+1} - 2U_{\ell mn} + U_{\ell mn-1}}{h_z^2}.$$

is the discrete Laplacian in three dimensions. The boundary conditions are

$$U_{0mn} = U_{Lmn} = U_{\ell 0n} = U_{\ell Mn} = U_{\ell m0} = U_{\ell mN} = 0.$$

3.3.1 Matrix-vector form

The major challenge of the finite-difference approach in solving Equation 2.8 is constructing the finite-difference matrix and associated load and solution vectors. To accomplish this, consider the three-dimensional domain as $M+1$ stacked slices of a two-dimensional domain in the $xz-$plane, which is of size $(N+1) \times (L+1)$. Since the boundary conditions are zero in all axes, this amounts to solving a $(L-1)(M-1)(N-1) \times (L-1)(M-1)(N-1)$ dimensional system of equations, defined by Equation 3.7. For example, $m = \ell = n = 1$ defines the first equation in this linear system,

$$\frac{U_{211} - 2U_{111} + U_{011}}{h_x^2} + \frac{U_{121} - 2U_{111} + U_{101}}{h_y^2} + \frac{U_{112} - 2U_{111} + U_{110}}{h_z^2} = -4\pi\gamma f_{111},$$

where $U_{011} = U_{101} = U_{110} = 0$ and f_{111} are known. To construct the matrix-vector form of Equation 3.7 we define

$$\mathbf{u}_{\ell m} = [U_{\ell m1} \ldots U_{\ell mN-1}]^T, \quad \text{and} \quad \mathbf{f}_{\ell m} = [f_{\ell m1} \ldots f_{\ell mN-1}]^T$$

for fixed $1 \leq \ell \leq L-1$ and $1 \leq m \leq M-1$. Then, our solution and load vectors are constructed by stacking the $N-1$ dimensional vectors $\mathbf{u}_{\ell m}$ and $\mathbf{f}_{\ell m}$ for all ℓ and m, yielding

$$\mathbf{U} = [\mathbf{u}_{11}\mathbf{u}_{21}\dots\mathbf{u}_{L-11}\dots\mathbf{u}_{1M-1}\mathbf{u}_{2M-1}\dots\mathbf{u}_{L-1M-1}]^T, \quad \text{and} \tag{3.8}$$

$$\mathbf{F} = [\mathbf{f}_{11}\mathbf{f}_{21}\dots\mathbf{f}_{L-11}\dots\mathbf{f}_{1M-1}\mathbf{f}_{2M-1}\dots\mathbf{f}_{L-1M-1}]^T.$$

We are effectively defining the computational domain as a series of 2D matrices stacked in y, where the rows of each matrix are defined in z and the columns in x. Starting with the first 2D matrix, we define the ordering of our solution and load vectors by stacking successive columns of each 2D matrix, forming column vectors. Based on the ordering of these vectors, our finite-difference matrix $\mathbf{A}$ can be expressed as a sparse, block tridiagonal matrix

$$\mathbf{A} = \begin{bmatrix} \mathbf{A}' & \mathbf{E} & & \mathbf{0} \\ \mathbf{E} & \ddots & \ddots & \\ & \ddots & \ddots & \mathbf{E} \\ \mathbf{0} & & \mathbf{E} & \mathbf{A}' \end{bmatrix}, \tag{3.9}$$

where the block matrix on the main diagonal is given by

$$\mathbf{A}' = \begin{bmatrix} \mathbf{D} & \mathbf{C} & & \mathbf{0} \\ \mathbf{C} & \ddots & \ddots & \\ & \ddots & \ddots & \mathbf{C} \\ \mathbf{0} & & \mathbf{C} & \mathbf{D} \end{bmatrix}, \tag{3.10}$$

with

$$\mathbf{D} = \begin{bmatrix} \left(-\frac{2}{h_z^2}-\frac{2}{h_x^2}-\frac{2}{h_y^2}\right) & \frac{1}{h_z^2} & & 0 \\ \frac{1}{h_z^2} & \ddots & \ddots & \\ & \ddots & \ddots & \frac{1}{h_z^2} \\ 0 & & \frac{1}{h_z^2} & \left(-\frac{2}{h_z^2}-\frac{2}{h_x^2}-\frac{2}{h_y^2}\right) \end{bmatrix}, \quad \text{and} \quad \mathbf{C} = \begin{bmatrix} \frac{1}{h_x^2} & & & 0 \\ & \ddots & & \\ & & \ddots & \\ 0 & & & \frac{1}{h_x^2} \end{bmatrix}$$

and the block matrix on the sub- and super-diagonal is

$$\mathbf{E} = \begin{bmatrix} \frac{1}{h_y^2} & & & 0 \\ & \ddots & & \\ & & \ddots & \\ 0 & & & \frac{1}{h_y^2} \end{bmatrix}.$$

With this formulation, we find that zero entries must be inserted into the $1/h_z^2$ and $1/h_x^2$ diagonals within $\mathbf{A}'$, due to the zero Dirichlet boundary conditions. The location of the zero entries for the $1/h_z^2$ diagonals lie between the ends of the sub- and super-diagonals (with entries $1/h_z^2$) of $\mathbf{D}$, between sequential $\mathbf{D}$ matrix blocks. This region is also defined by the lower left (for the super-diagonal in $\mathbf{D}$) and the upper right (for the sub-diagonal in $\mathbf{D}$) corners of the sub- and super-diagonal block matrix $\mathbf{C}$. For the zero entries in the $1/h_x^2$ diagonals, view the structure of the matrix $\mathbf{A}$ in the same way as $\mathbf{A}'$ in Equation 3.10, and the result follows the same as for the $1/h_z^2$ diagonals.

Recall that the entries of $\mathbf{F}$ are defined as

$$f_{\ell mn} \approx f(x_\ell, y_m, z_n) = \frac{\partial \rho(x_\ell, y_m, z_n)}{\partial z}, \tag{3.11}$$

for $1 \leq \ell \leq L-1$, $1 \leq m \leq M-1$, and $1 \leq n \leq N-1$. In order to obtain values f_{mn} in our linear system, we apply a central difference approximation to the derivative in Equation 3.11 as follows,

$$\frac{\partial \rho(x_\ell, y_m, z_n)}{\partial z} \approx \frac{\rho(x_\ell, y_m, z_{n+1}) - \rho(x_\ell, y_m, z_{n-1})}{2h_z}.$$

Even though ρ is not continuous, the central difference approximation—and hence the derivative—is only evaluated on the continuous segments of the density function. In our numerical approximation, we assume constant density values within each cell of the grid; as such, these continuous segments are defined by each cell in the computational domain.

Therefore, Equations 3.8 and 3.9 yield the matrix-vector form of Equation 3.7,

$$\mathbf{AU} = \mathbf{F}.$$

This system is then approximated iteratively using a conjugate gradient method, computing a solution for the component of gravitational acceleration simultaneously at every point in the domain.

3.4 Summary

This chapter outlined the finite-difference scheme for computing a direct solution to gravitational acceleration in two and three dimensions. We use zero Dirichlet boundary conditions for three-dimensional direct finite-difference solutions since our two-dimensional results demonstrated that solutions with zero Dirichlet and Robin boundary conditions were equivalent. We also described in detail the structure of linear system that results from computing this numerical solution. In the next chapter, we outline the two- and three-dimensional finite-volume formulation of our direct solution.

CHAPTER 4

FINITE-VOLUME SCHEME

A finite-volume scheme is also implemented to numerically compute the vertical component of the gravitational field. This numerical method was chosen for two main reasons; to analytically remove the derivative of the piecewise continuous density function, and also to provide a starting point for future work implementing unstructured grids to model the computational domain. We first discuss the theory involved in applying this scheme in two and then three dimensions based on the techniques used in reference [16], with the ultimate objective being to test the solution on simple three-dimensional source regions. The matrix-vector formulations of the two- and three-dimensional schemes are explained, and a brief discussion on different mesh options available for finite-volume methods is included.

4.1 Boundary conditions

In both the two- and three-dimensional formulations of this scheme, zero Robin boundary conditions are used. Recall that we have assumed $\alpha = 1$ in Equation 2.9. We compute these boundary conditions numerically using a central difference approximation for the normal derivative term. To illustrate an example, for a one-dimensional problem with numerical solution $u_i = u(x_i)$, the Robin boundary condition on a discretized domain can be expressed as

$$u_i + \frac{u_{i+1} - u_{i-1}}{2} = 0.$$

For points x_i near the boundaries, the value of the solution at u_{i+1} and u_{i-1} is determined by the condition given above. Solving this expression for these quantities, we obtain

$$u_{i+1} = u_{i-1} - 2u_i, \quad \text{and} \quad u_{i-1} = u_{i+1} + 2u_i.$$

The relations above are extended to two and three dimensions in the finite-volume scheme discussed below. For zero Dirichlet conditions, u_{i+1} and u_{i-1} are simply taken to be zero.

4.2 Two dimensional scheme

In two dimensions, we define the computational domain $\Omega = (\alpha, \beta) \times (\gamma, \delta)$, with $\alpha < \beta, \gamma < \delta$, and $\alpha, \beta, \gamma, \delta \in \mathbb{R}$. Now, $g_z = g_z(x, z)$, $\rho = \rho(x, z)$, and

$$\nabla^2 g_z = \frac{\partial^2 g_z}{\partial x^2} + \frac{\partial^2 g_z}{\partial z^2},$$

leading to the governing equation

$$\frac{\partial^2 g_z(x,z)}{\partial x^2} + \frac{\partial^2 g_z(x,z)}{\partial z^2} = -a\frac{\partial \rho(x,z)}{\partial z}, \quad (x,z) \in \Omega. \tag{4.1}$$

Define a mesh of $N_1 \times N_2$ cells, where N_1 and N_2 are integers, over Ω such that

$$x_0 = x_{\frac{1}{2}} = \alpha < x_1 < \ldots < x_{i-\frac{1}{2}} < x_i < x_{i+\frac{1}{2}} < \ldots < x_{N_1} < x_{N_1+\frac{1}{2}} = x_{N_1+1} = \beta,$$

$$z_0 = z_{\frac{1}{2}} = \gamma < z_1 < \ldots < z_{j-\frac{1}{2}} < z_j < z_{j+\frac{1}{2}} < \ldots < z_{N_2} < z_{N_2+\frac{1}{2}} = z_{N_2+1} = \delta,$$

and $h_i = x_{i+\frac{1}{2}} - x_{i-\frac{1}{2}}$, $\ell_j = z_{j+\frac{1}{2}} - z_{j-\frac{1}{2}}$. According to the finite-volume formulation, the control volumes are defined by

$$K_{i,j} = [x_{i-\frac{1}{2}}, x_{i+\frac{1}{2}}] \times [z_{j-\frac{1}{2}}, z_{j+\frac{1}{2}}],$$

and the vertical component of gravitational acceleration is computed at the center of each control volume using an $N_1 \times N_2$ system of equations. In two dimensions, we the system of equations is defined by integrating Equation 4.1 over each control volume, that is,

$$\int_{K_{i,j}} \left[\frac{\partial^2 g_z(x,z)}{\partial x^2} + \frac{\partial^2 g_z(x,z)}{\partial z^2} \right] = -a \int_{K_{i,j}} \frac{\partial \rho(x,z)}{\partial z}, \quad i = 1, \ldots, N_1, j = 1, \ldots, N_2.$$

Since we are working in two dimensions, integrating over the control volumes should be interpreted as evaluating the integrand within a double integral, one in x and the other in z:

$$\int_x \int_z \left[\frac{\partial^2 g_z(x,z)}{\partial x^2} + \frac{\partial^2 g_z(x,z)}{\partial z^2} \right] = -a \int_x \int_z \frac{\partial \rho(x,z)}{\partial z}, \quad i = 1, \ldots, N_1, j = 1, \ldots, N_2. \tag{4.2}$$

Note that these are definite integrals, with $x \in (x_{i-\frac{1}{2}}, x_{i+\frac{1}{2}})$ and $z \in (z_{j-\frac{1}{2}}, z_{j+\frac{1}{2}})$. Separating the two terms on the left-hand side of Equation 4.2 and evaluating each using the Fundamental Theorem of Calculus gives

$$\int_z \left[\frac{\partial g_z(x_{i+\frac{1}{2}}, z)}{\partial x} - \frac{\partial g_z(x_{i-\frac{1}{2}}, z)}{\partial x}\right] + \int_x \left[\frac{\partial g_z(x, z_{j+\frac{1}{2}})}{\partial z} - \frac{\partial g_z(x, z_{j-\frac{1}{2}})}{\partial z}\right]. \tag{4.3}$$

Turning to the right-hand side of Equation 4.2, the integral is approximated using the trapezoidal quadrature rule, yielding

$$\begin{aligned} -a\int_x \left[\rho(x, z_{j+\frac{1}{2}}) - \rho(x, z_{j-\frac{1}{2}})\right] = -\frac{ah_i}{2}\Bigg\{ &\left[\rho(x_{i-\frac{1}{2}}, z_{j+\frac{1}{2}}) - \rho(x_{i-\frac{1}{2}}, z_{j-\frac{1}{2}})\right] \\ &+ \left[\rho(x_{i+\frac{1}{2}}, z_{j+\frac{1}{2}}) - \rho(x_{i+\frac{1}{2}}, z_{j-\frac{1}{2}})\right]\Bigg\} \end{aligned}$$

4.2.1 Matrix-vector form

The left-hand side integrals given in Equation 4.3 are evaluated using a central difference approximation for the integrand, and then applying the mean value theorem for integrals. The mean value theorem states that the definite integral is equivalent to the integrand evaluated at the mean value of the limits of integration—in our case, x_i and z_j—multiplied by the length of the interval, denoted by h_i and ℓ_j. Hence, Equation 4.3 is approximated by

$$F_{i+\frac{1}{2},j} - F_{i-\frac{1}{2},j} + F_{i,j+\frac{1}{2}} - F_{i,j-\frac{1}{2}} \tag{4.4}$$

with $u_{i,j}$ taken to be an approximation of g_z in each control volume $K_{i,j}$, $i = 1, \ldots, N_1, j = 1, \ldots, N_2$:

$$\begin{aligned} F_{i+\frac{1}{2},j} &:= \ell_j \frac{u_{i+1,j} - u_{i,j}}{h_{i+\frac{1}{2}}}, \\ F_{i-\frac{1}{2},j} &:= \ell_j \frac{u_{i,j} - u_{i-1,j}}{h_{i-\frac{1}{2}}}, \\ F_{i,j+\frac{1}{2}} &:= h_i \frac{u_{i,j+1} - u_{i,j}}{\ell_{j+\frac{1}{2}}}, \end{aligned}$$

and,

$$F_{i,j-\frac{1}{2}} := h_i \frac{u_{i,j} - u_{i,j-1}}{\ell_{j-\frac{1}{2}}}.$$

Setting

$$f_{i,j} = \Big[\rho(x_{i+\frac{1}{2}}, z_{j+\frac{1}{2}}) - \rho(x_{i+\frac{1}{2}}, z_{j-\frac{1}{2}})\Big] - \Big[\rho(x_{i-\frac{1}{2}}, z_{j+\frac{1}{2}}) - \rho(x_{i-\frac{1}{2}}, z_{j-\frac{1}{2}})\Big], \tag{4.5}$$

the finite-volume scheme used to solve Equation 4.1 is defined by combining the left-hand side and right-hand side expressions given in Equations 4.4 and 4.5, yielding

$$F_{i+\frac{1}{2},j} - F_{i-\frac{1}{2},j} + F_{i,j+\frac{1}{2}} - F_{i,j-\frac{1}{2}} = -ah_i f_{i,j},$$

subject to zero Robin boundary conditions,

$$u_{0,j} = 2h_{i+\frac{1}{2}} u_{1,j} + u_{2,j},$$

$$u_{N_1+1,j} = u_{N_1-1,j} - 2h_{i-\frac{1}{2}} u_{N_1,j},$$

$$u_{i,0} = 2\ell_{j+\frac{1}{2}} u_{i,1} + u_{i,2},$$

$$u_{i,N_2+1} = u_{i,N_2-1} - 2\ell_{j-\frac{1}{2}} u_{i,N_2},$$

$$i = 1, \ldots, N_1, j = 1, \ldots, N_2.$$

The matrix-vector form of this scheme can be represented by

$$\mathbf{Ax} = \mathbf{b}$$

where $\mathbf{x}$ is formed by stacking the column vectors $\mathbf{u}_i = [u_{i,1}, \ldots, u_{i,N_2}]^T, i = 1, \ldots, N_1$ (since z is positive downward, these elements form the rows of the matrix, while the elements in x form the columns):

$$\mathbf{x} = [\mathbf{u}_1, \ldots, \mathbf{u}_{N_1}]^T.$$

The vector $\mathbf{b}$ is constructed in a similar fashion, where $\mathbf{f}_i = [f_{i,1}, \ldots, f_{i,N_2}]^T$, $i = 1, \ldots, N_1$ are vector elements of

$$\mathbf{b} = [\mathbf{f}_1, \ldots, \mathbf{f}_{N_1}]^T.$$

4.3 Three dimensional scheme

A three-dimensional finite volume scheme is also implemented to numerically compute the vertical component of the gravitational field. In this case, take the vertical component of the gravitational field,

$$\nabla^2 g_z = -a\frac{\partial \rho}{\partial z}, \tag{4.6}$$

where $a = 4\pi\gamma$, γ the universal gravitational constant, with Robin boundary conditions. In three dimensions, Equation 4.6 is defined on the parallelepiped $\Omega = (\alpha, \beta)\times(\gamma, \delta)\times(\epsilon, \zeta)$, with $\alpha < \beta, \gamma < \delta, \epsilon < \zeta$ and $\alpha, \beta, \gamma, \delta, \epsilon, \zeta \in \mathbb{R}$. In three dimensions, $g_z = g_z(x, y, z), \rho = \rho(x, y, z)$, and

$$\nabla^2 g_z = \frac{\partial^2 g_z}{\partial x^2} + \frac{\partial^2 g_z}{\partial y^2} + \frac{\partial^2 g_z}{\partial z^2},$$

which gives a governing equation of

$$\frac{\partial^2 g_z(x, y, z)}{\partial x^2} + \frac{\partial^2 g_z(x, y, z)}{\partial y^2} + \frac{\partial^2 g_z(x, y, z)}{\partial z^2} = -a\frac{\partial \rho(x, y, z)}{\partial z}, \quad (x, y, z) \in \Omega. \tag{4.7}$$

Define a mesh of $N_1 \times N_2 \times N_3$ cells over Ω such that

$$x_0 = x_{\frac{1}{2}} = \alpha < x_1 < \ldots < x_{i-\frac{1}{2}} < x_i < x_{i+\frac{1}{2}} < \ldots < x_{N_1} < x_{N_1+\frac{1}{2}} = x_{N_1+1} = \beta,$$

$$y_0 = y_{\frac{1}{2}} = \gamma < y_1 < \ldots < y_{j-\frac{1}{2}} < y_j < y_{j+\frac{1}{2}} < \ldots < y_{N_2} < y_{N_2+\frac{1}{2}} = y_{N_2+1} = \delta,$$

$$z_0 = z_{\frac{1}{2}} = \epsilon < z_1 < \ldots < z_{k-\frac{1}{2}} < z_k < z_{k+\frac{1}{2}} < \ldots < z_{N_3} < z_{N_3+\frac{1}{2}} = z_{N_3+1} = \zeta,$$

and $h_i = x_{i+\frac{1}{2}} - x_{i-\frac{1}{2}}$, $\ell_j = y_{j+\frac{1}{2}} - y_{j-\frac{1}{2}}$, and $m_k = z_{k+\frac{1}{2}} - z_{k-\frac{1}{2}}$. Hence, the control volumes are defined by

$$K_{i,j,k} = [x_{i-\frac{1}{2}}, x_{i+\frac{1}{2}}] \times [y_{j-\frac{1}{2}}, y_{j+\frac{1}{2}}] \times [z_{k-\frac{1}{2}}, z_{k+\frac{1}{2}}],$$

and compute the vertical gravitational acceleration at the center of each control volume by a $N_1 \times N_2 \times N_3$ system of equations. These equations are defined by integrating Equation 4.7 over each control volume, that is,

$$\int_{K_{i,j,k}} \left[\frac{\partial^2 g_z(x,y,z)}{\partial x^2} + \frac{\partial^2 g_z(x,y,z)}{\partial y^2} + \frac{\partial^2 g_z(x,y,z)}{\partial z^2} \right] = -a \int_{K_{i,j,k}} \frac{\partial \rho(x,y,z)}{\partial z},$$

$$i = 1, \ldots, N_1, j = 1, \ldots, N_2, k = 1, \ldots, N_3.$$

The integral over $K_{i,j,k}$ can be interpreted as a triple integral in x, y, and z:

$$\int_x \int_y \int_z \left[\frac{\partial^2 g_z(x,y,z)}{\partial x^2} + \frac{\partial^2 g_z(x,y,z)}{\partial y^2} + \frac{\partial^2 g_z(x,y,z)}{\partial z^2} \right] = -a \int_x \int_y \int_z \frac{\partial \rho(x,y,z)}{\partial z},$$

$$i = 1, \ldots, N_1, j = 1, \ldots, N_2, k = 1, \ldots, N_3,$$

where each integral is a definite integral with $x \in (x_{i-\frac{1}{2}}, x_{i+\frac{1}{2}})$, $y \in (y_{j-\frac{1}{2}}, y_{j+\frac{1}{2}})$, and $z \in (z_{k-\frac{1}{2}}, z_{k+\frac{1}{2}})$. Separating the three terms on the left-hand side integral and evaluating under the Fundamental Theorem of Calculus gives

$$\int_y \int_z \left[\frac{\partial g_z(x_{i+\frac{1}{2}}, y, z)}{\partial x} - \frac{\partial g_z(x_{i-\frac{1}{2}}, y, z)}{\partial x} \right] + \int_x \int_z \left[\frac{\partial g_z(x, y_{j+\frac{1}{2}}, z)}{\partial y} - \frac{\partial g_z(x, y_{j-\frac{1}{2}}, z)}{\partial y} \right]$$
$$+ \int_x \int_y \left[\frac{\partial g_z(x, y, z_{k+\frac{1}{2}})}{\partial z} - \frac{\partial g_z(x, y, z_{k-\frac{1}{2}})}{\partial z} \right],$$

and evaluating the right-hand side under the Fundamental Theorem of Calculus followed by the trapezoidal quadrature rule to approximate the integrals:

$$\begin{aligned} -a \int_x \int_y \left[\rho(x,y,z_{k+\frac{1}{2}}) - \rho(x,y,z_{k-\frac{1}{2}}) \right] = -\frac{a h_i \ell_j}{4} \Bigg\{ & \left[\rho(x_{i-\frac{1}{2}}, y_{j-\frac{1}{2}}, z_{j+\frac{1}{2}}) - \rho(x_{i-\frac{1}{2}}, y_{j-\frac{1}{2}}, z_{j+\frac{1}{2}}) \right] \\ & + \left[\rho(x_{i-\frac{1}{2}}, y_{j+\frac{1}{2}}, z_{j+\frac{1}{2}}) - \rho(x_{i-\frac{1}{2}}, y_{j+\frac{1}{2}}, z_{j-\frac{1}{2}}) \right] \\ & + \left[\rho(x_{i+\frac{1}{2}}, y_{j-\frac{1}{2}}, z_{j+\frac{1}{2}}) - \rho(x_{i+\frac{1}{2}}, y_{j-\frac{1}{2}}, z_{j-\frac{1}{2}}) \right] \\ & + \left[\rho(x_{i+\frac{1}{2}}, y_{j+\frac{1}{2}}, z_{j+\frac{1}{2}}) - \rho(x_{i+\frac{1}{2}}, y_{j+\frac{1}{2}}, z_{j-\frac{1}{2}}) \right] \Bigg\} \end{aligned}$$

4.3.1 Matrix-vector form

The left-hand side double integrals are evaluated using a central difference approximation for the integrand, and then by applying the mean value theorem for integrals. Hence, the finite-volume scheme for solving Equation 4.7 is given by

$$F_{i+\frac{1}{2},j,k} - F_{i-\frac{1}{2},j,k} + F_{i,j+\frac{1}{2},k} - F_{i,j-\frac{1}{2},k} + F_{i,j,k+\frac{1}{2}} - F_{i,j,k-\frac{1}{2}} = -ah_i\ell_j f_{i,j,k} \tag{4.8}$$

where

$$F_{i+\frac{1}{2},j,k} := \ell_j m_k \frac{u_{i+1,j,k} - u_{i,j,k}}{h_{i+\frac{1}{2}}},$$

$$F_{i-\frac{1}{2},j,k} := \ell_j m_k \frac{u_{i,j,k} - u_{i-1,j,k}}{h_{i-\frac{1}{2}}},$$

$$F_{i,j+\frac{1}{2},k} := h_i m_k \frac{u_{i,j+1,k} - u_{i,j,k}}{\ell_{j+\frac{1}{2}}},$$

$$F_{i,j-\frac{1}{2},k} := h_i m_k \frac{u_{i,j,k} - u_{i,j-1,k}}{\ell_{j-\frac{1}{2}}},$$

$$F_{i,j,k+\frac{1}{2}} := h_i \ell_j \frac{u_{i,j,k+1} - u_{i,j,k}}{m_{k+\frac{1}{2}}},$$

$$F_{i,j,k-\frac{1}{2}} := h_i \ell_j \frac{u_{i,j,k} - u_{i,j,k-1}}{m_{k-\frac{1}{2}}},$$

and

$$f_{i,j,k} = \rho(x_i, y_j, z_{k+\frac{1}{2}}) - \rho(x_i, y_j, z_{k-\frac{1}{2}}),$$

which is subject to the zero Robin boundary condition

$$u_{0,j,k} = 2h_{i+\frac{1}{2}} u_{1,j,k} + u_{2,j,k},$$

$$u_{N_1+1,j,k} = u_{N_1-1,j,k} - 2h_{i-\frac{1}{2}} u_{N_1,j,k},$$

$$u_{i,0,k} = 2\ell_{j+\frac{1}{2}} u_{i,1,k} + u_{i,2,k},$$

$$u_{i,N_2+1,k} = u_{i,N_2-1,k} - 2\ell_{j-\frac{1}{2}} u_{i,N_2,k},$$

$$u_{i,j,0} = 2m_{k+\frac{1}{2}} u_{i,j,1} + u_{i,j,2},$$

$$u_{i,j,N_3+1} = u_{i,j,N_3-1} - 2m_{k-\frac{1}{2}} u_{i,j,N_3},$$

$$i = 1, \ldots, N_1, j = 1, \ldots, N_2, k = 1, \ldots, N_3.$$

Again, here the approximation $u_{i,j,k}$ is used to estimate the value of g_z in the control volumes $K_{i,j,k}$, $i = 1, \ldots, N_1, j = 1, \ldots, N_2, k = 1, \ldots, N_3$. The numerical scheme given in Equation 4.8 can be expressed in matrix-vector form as

$$\mathbf{Ax} = \mathbf{b}.$$

To form the vector $\mathbf{x}$, the column vectors of the solution in the x dimension are stacked for each y value in sequence,

$$\mathbf{u}_{i,j} = [u_{i,j,1}, \ldots, u_{i,j,N_3}]^T, \quad i = 1, \ldots, N_1, j = 1, \ldots, N_2$$

forming

$$\mathbf{x} = [\mathbf{u}_{1,1}, \mathbf{u}_{2,1}, \ldots, \mathbf{u}_{N_1,1}, \ldots, \mathbf{u}_{1,N_2}, \mathbf{u}_{2,N_2}, \ldots, \mathbf{u}_{N_1,N_2}]^T.$$

The vector $\mathbf{b}$ is constructed in the same manner, ultimately yielding

$$\mathbf{b} = [\mathbf{f}_{1,1}, \mathbf{f}_{2,1}, \ldots, \mathbf{f}_{N_1,1}, \ldots, \mathbf{f}_{1,N_2}, \mathbf{f}_{2,N_2}, \ldots, \mathbf{f}_{N_1,N_2}]^T,$$

where

$$\mathbf{f}_{i,j} = [f_{i,j,1}, \ldots, f_{i,j,N_3}]^T, \quad i = 1, \ldots, N_1, j = 1, \ldots, N_2.$$

4.4 Mesh considerations

There are many options for mesh discretization under the finite-volume method; in fact, one main advantage of this numerical method is that it easily accommodates unstructured grids. Unstructured grids better model the shape of bodies, and do so using fewer cells than regular meshes. This feature also allows the solution to be computed on a physical domain of any shape. Additionally, mesh refinement is performed more efficiently in unstructured grids versus regular grids. Some examples of unstructured grids include tetrahedral meshes, Voronoi meshes, and Delaunay meshes; see reference [12] for discussion and application

of these meshes to gravity forward models. For rectangular or parallelepiped domains, a finite-volume scheme may be applied with structured rectangular or parallelepipedic control volumes. Here, the mesh is expressed as a two- or three-dimensional array. Our study is intended as a first look into the direct solution method, we use a structured parallelepipedic mesh for our example problems. This will allow our finite-volume solution to be readily compared with previously obtained finite-difference solutions.

4.5 Summary

In this chapter we described the finite-volume formulation of the direct solution in both two and three dimensions. We first discussed how we computed the Robin boundary conditions in the context of this scheme, and then moved to the specifics of simplifying the governing equation to formulate the linear system. The structure of the matrix-vector form of this solution was also described. Finally, we mentioned some options for mesh discretization that are available in finite-volume methods in general. In the next chapter, we apply the direct solution under both finite-difference and finite-volume schemes to example problems, and conduct comparisons between these and traditional solutions.

CHAPTER 5

RESULTS

In this chapter we compare numerical results obtained using the direct solution to numerical differentiation and integral solutions. Integral solutions are known to give accurate results for three-dimensional gravity anomaly models, and numerical differentiation methods have been established as suitable alternatives for problems with a large number of computation points. These solutions are compared with the direct solution for three-dimensional synthetic problems. The direct solution is then applied to more realistic models.

5.1 Synthetic problems

The synthetic examples in this section are used to establish baseline results for forward modeling gravitational acceleration using the direct solution; the direct solution will be applied to a real data set in Section 5.2. Before comparing the direct solution with the integral and numerical differentiation results, the convergence of the direct finite-difference and finite-volume solutions is established on a small test domain. Then, the direct and numerical differentiation solutions are computed for a synthetic problem with cubic source geometry. Finally, through an application to a synthetic borehole problem, the accuracy of the direct solutions is established by comparison with the integral solution.

5.1.1 Convergence of direct solution

The vertical component of gravitational acceleration was computed for a small three-dimensional test problem. This solution represents the closest numerical approximation to the true gravitational acceleration component solution for the given problem. The convergence tests were conducted on the domain $\Omega_1 = \{(x, y, z) \in \mathbb{R}^3 : 0 \leq x \leq 10, 0 \leq y \leq 10, 0 \leq z \leq 10\}$ with a source of density 1.0 g/cm^3 defined on the cube $(x, y, z) \in (4, 4, 4) : (6, 6, 6)$.

Gravity values were computed and the results compared for increasingly fine meshes. The numerical solutions are converged when the results between two mesh sizes match visually.

Figure 5.1 illustrates the convergence of the direct finite-difference solution, and Figure 5.2 illustrates the convergence of the direct finite-volume solution. The finite-difference solution is converged for $200 \times 200 \times 200$ grid points while the finite-volume solution converges with $80 \times 80 \times 80$ grid points. This means that to obtain an accurate numerical result, the finite-volume solution requires fewer grid points than the finite-difference solution.

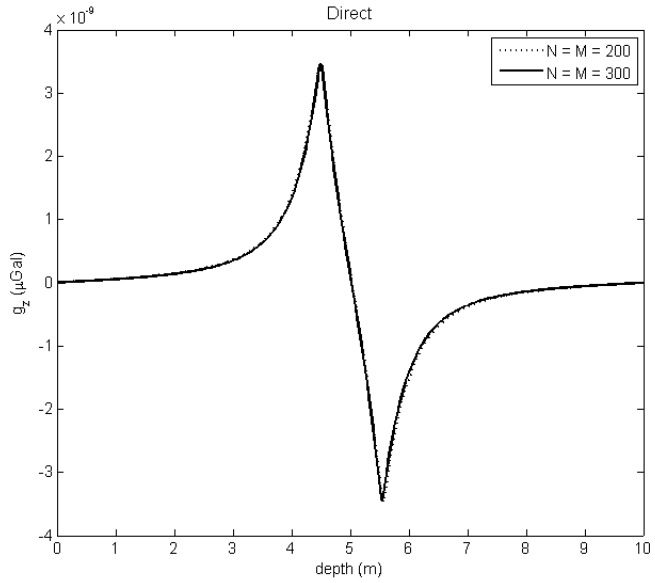

Figure 5.1: Convergence of direct finite-difference solution of the vertical component of gravitational acceleration on Ω_1. Vertical line plot taken for $(x, y) = (5, 5)$. Solution converges for $200 \times 200 \times 200$ grid points.

5.1.2 Accuracy of direct solution

A three-dimensional synthetic borehole problem is used to determine the accuracy of the numerical solutions. This is accomplished by calculating the integral solution along the borehole in Figure 5.3 and comparing the result to the direct finite-difference and finite-volume solutions. Figure 5.4 shows how the three vertical component of gravitational acceleration solutions compare along the simulated borehole. Although there are discrepancies at the

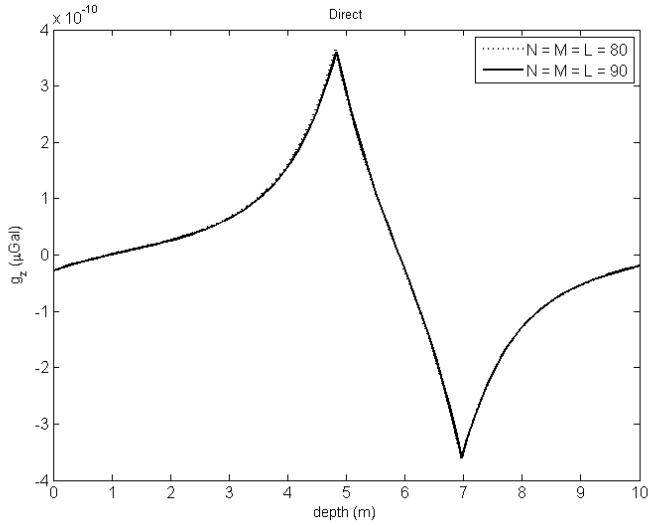

Figure 5.2: Convergence of direct finite-volume solution of the vertical component of gravitational acceleration on Ω_1. Vertical line plot taken for $(x, y) = (5, 5)$. Solution converges for $80 \times 80 \times 80$ grid points.

edges of the computational domain, there is excellent agreement within the source. It is also important to note that the direct finite-difference and finite-volume solutions agree exactly throughout the entire domain.

5.1.3 Comparison with numerical differentiation solution

Here, we compute the vertical component of gravitational acceleration produced by a simple three-dimensional source distribution. The direct finite-difference and finite-volume solutions are compared with the numerical differentiation solution by computing gravity values along vertical profiles that pass through the source region. The density model for this problem a cube with density 1.0 g/cm^3 located at $(x, y, z) \in (45, 45, 45) : (55, 55, 55)$, where the domain has zero background density. The computational domain is defined in meters by $\Omega = \{(x, y, z) \in \mathbb{R}^3 : 0 \leq x \leq 100, 0 \leq y \leq 100, 0 \leq z \leq 100\}$. The direct solutions are computed by finite-difference and finite-volume methods, yielding results for g_z, the vertical component of gravitational acceleration. For the numerical differentiation solution, the gravitational potential resulting from the model is computed, then centered difference

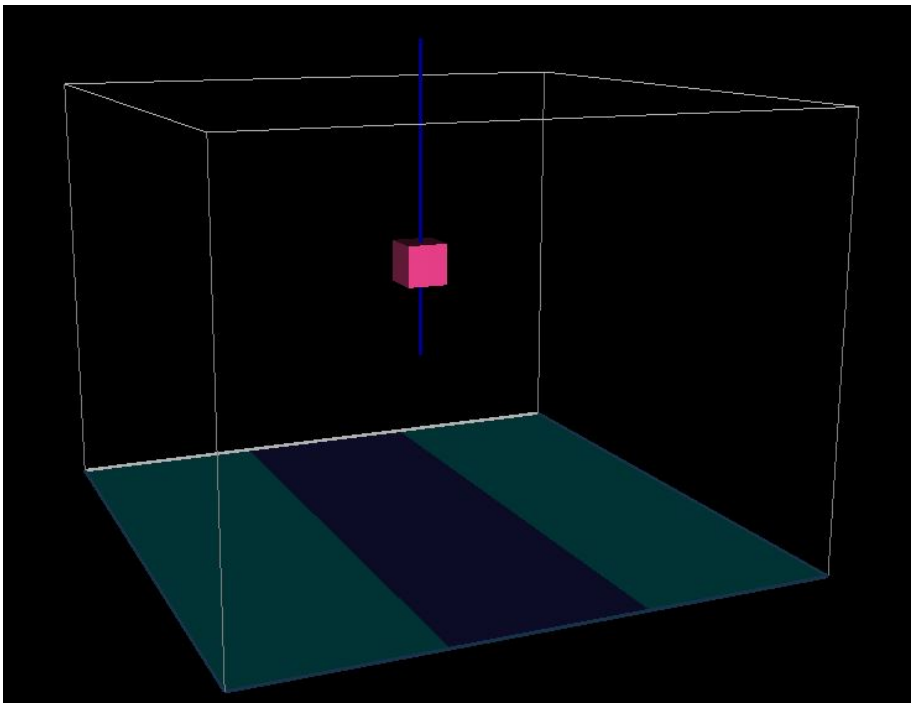

Figure 5.3: Synthetic density distribution for borehole simulations. Vertical borehole (in blue) passing through center of source with density 1.0 g/cm^3; zero background density.

approximations yield the g_z solution. Figure 5.5(a) illustrates a two-dimensional profile of the computational region, taken at $y = 50$. The vertical component of gravitational acceleration obtained through the three solution approaches are shown in Figure 5.5(b)$-$(d); the direct finite-difference and numerical differentiation solutions were computed using $240 \times 240 \times 240$ grid points, and the direct finite-volume solution was computed using $50 \times 50 \times 50$ grid points.

Vertical profiles through the source body are illustrated in Figure 5.6 to aid in visual comparison of the direct and numerical differentiation solutions; all three solutions seem to match closely. It should be noted that the direct finite-volume solution was computed using a significantly smaller grid than the other two solutions, which we expect based on the results of the convergence test. Using these data, we compute the error between the direct finite-difference and numerical differentiation solutions using the L_1 and L_∞ matrix norms. We find that the L_1-norm $= 4.59 \times 10^{-8}$ and the L_∞-norm $= 5.63 \times 10^{-10}$. In

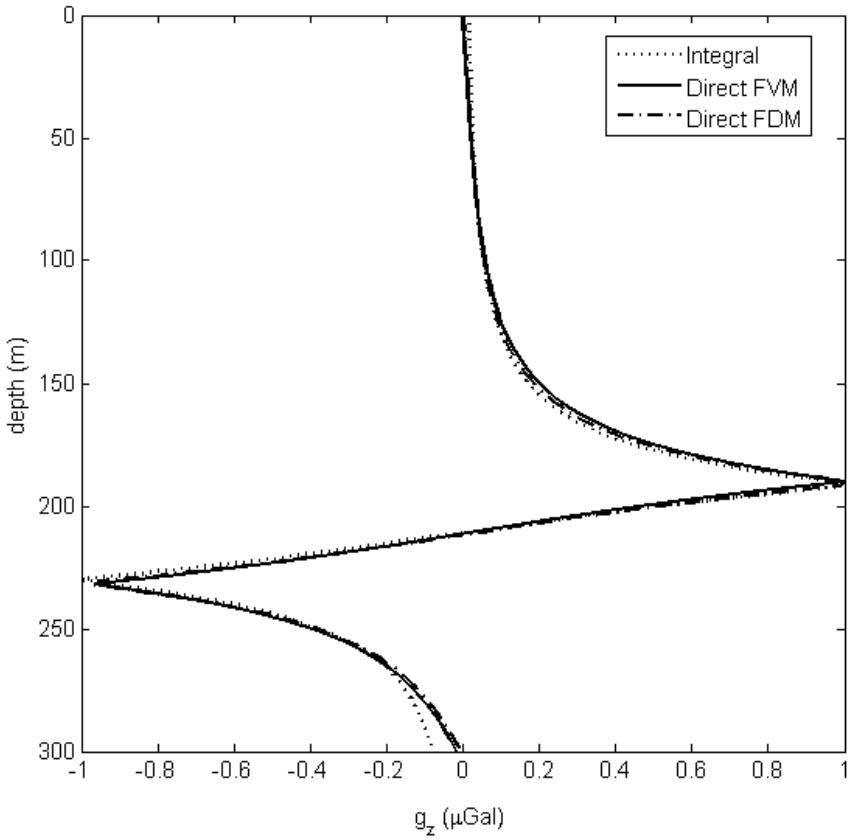

Figure 5.4: Borehole simulation solutions: integral (dash), direct finite-volume (solid), and direct finite-difference (dot-dash). Direct finite-volume solution produced using $80 \times 80 \times 80$ grid points; direct finite-difference solution computed using $200 \times 200 \times 200$ grid points.

determining these values, we have subtracted the numerical differentiation solution from the direct finite-difference solution. Since the direct finite-volume solution matches so closely with the direct finite-difference solution based on visual inspection, we infer that the error between this solution and the numerical differentiation solution is close to these values.

In this example we have compared two solutions of gravitational acceleration. The direct solution calculates the desired field immediately from the governing equation, and the numerical differentiation solution obtains gravitational potential from the governing equation, then approximates a derivative to obtain gravitational acceleration. Both solutions were computed using zero Dirichlet boundary conditions; that is, for the direct solution the boundary condition $g_z = 0$ was implemented, and for the numerical differentiation solution, $\phi = 0$ was imposed on the boundary. However, since $g_z = \partial\phi/\partial z$, this amounts to imposing a Cauchy condition on the solution, where the value of ϕ and $\partial\phi/\partial z$ are simultaneously specified for all points on the boundary. It has been shown, [17], that Poisson's equation is ill-posed under a Cauchy boundary condition. Hence, future implementations of this comparison should implement consistent boundary conditions—in this case, a Neumann condition when solving Poisson's equation for gravitational potential under the numerical differentiation approach.

5.2 Application

In the previous section, we implemented the direct solution for example problems with simple source geometries, and considered the results in comparison with benchmark integral and numerical differentiation solutions. We now apply the direct solution to modeling data from the Cranfield reservoir (see Figure 5.7), a carbon capture and sequestration test site located in southwest Mississippi. The finite-difference formulation of the direct solution was implemented in this application; we have previously demonstrated the equivalence of the finite-difference and finite-volume direct solutions in three dimensions. In this application, we also introduce a solution of the horizontal component of gravitational acceleration, computed

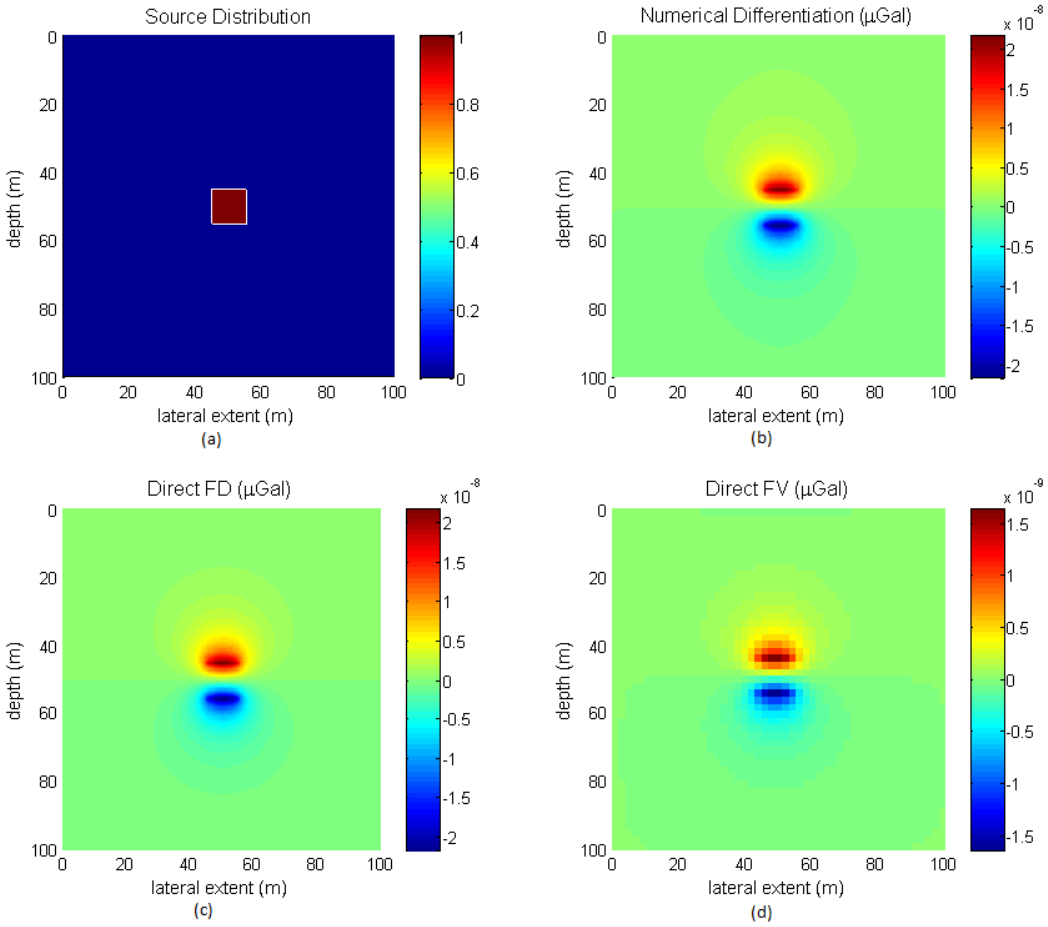

Figure 5.5: Solutions of the vertical component of gravitational acceleration. (a) Two-dimensional slice taken at $y = 50$ of three-dimensional source distribution Ω. (b) Numerical differentiation, (c) direct finite-difference, and (d) direct finite-volume solutions reported in μGal.

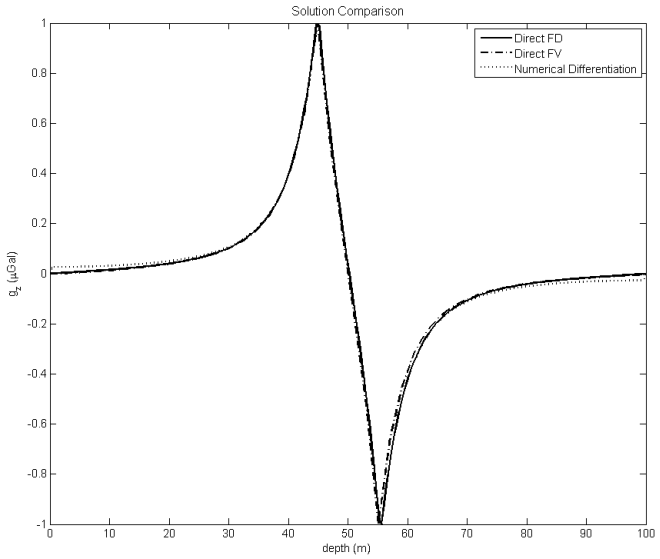

Figure 5.6: Solutions of the vertical component of gravitational acceleration. Vertical line plots taken at $(x, y) = (50, 50)$ through the center of the three-dimensional source in Ω. Numerical differentiation (dash), direct finite-difference (solid), and direct finite-volume (dot-dash) solutions reported in μGal.

in the x dimension. This information will aid in interpreting the location and geometry of the region of interest by resolving the sides of the reservoir.

Density data from a two-dimensional slice of the Cranfield reservoir was duplicated in a third dimension to simulate a realistic three-dimensional reservoir intended to mimic the full Cranfield reservoir. A two-dimensional profile of the density data taken through the center of the body is shown in Figure 5.8. Note that the density values in this problem are negative. This means that, for example, in a vertical component solution, a gravity low resolves the top of the source instead of a gravity high. The vertical and horizontal components of gravitational acceleration are computed, and the vertical component solution is also shown for the borehole depicted in Figure 5.7. As seen in Figure 5.9(a) and Figure 5.9(b), the vertical and horizontal component solutions resolve the orientation of the source in space. The vertical component of gravitational acceleration solution is simulated along a borehole passing through the reservoir (see Figure 5.10). The peaks are not defined as sharply as

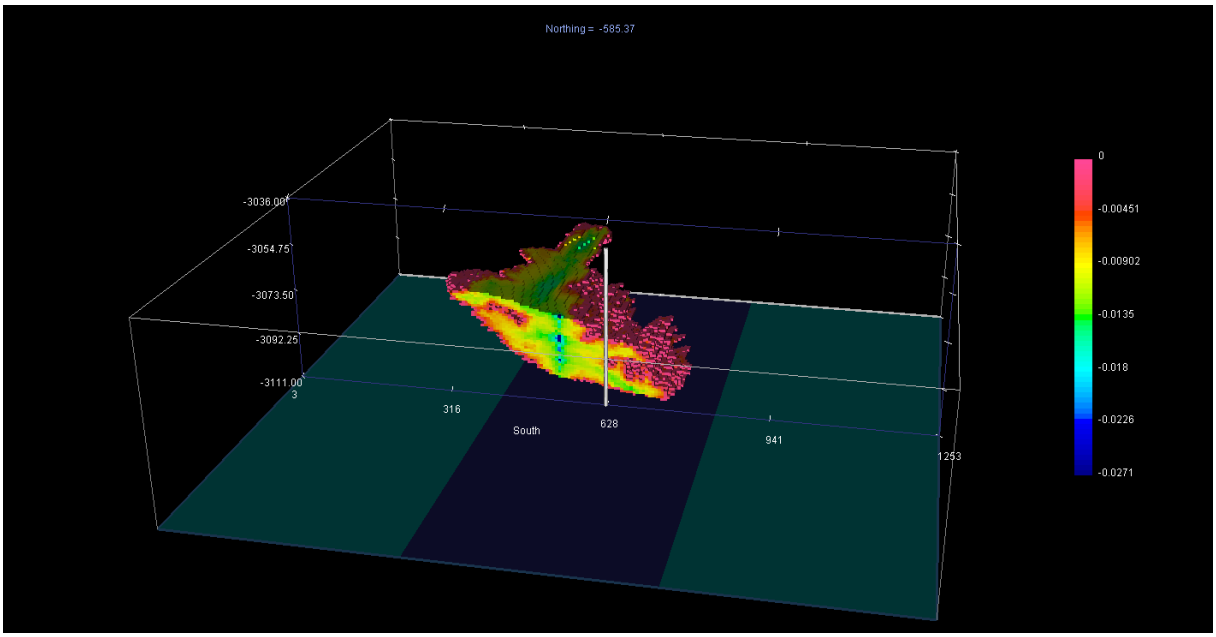

Figure 5.7: Full Cranfield reservoir model illustrating two-dimensional data profile. Density data reported in negative values with units g/cm^3; zero background density. Borehole located at $x = 585$.

those in the synthetic examples; this is due to the geometric complexity of the source. Note that the magnitude of these gravitational acceleration solutions differs from earlier examples by $\sim 10^{-3}$; this occurs because the source distribution in this problem has units on the order of 10^{-3} compared to our synthetic problems.

5.3 Summary

Here, we have applied the direct solution to three-dimensional synthetic example problems and to one real data set. We began by determing the difference in converged grid sizes between direct finite-difference and direct finite-volume solutions for a simple test problem. Then, we determined that the direct solutions are accurate in comparison with the integral form solution through a synthetic borehole model. Next, we compared the direct and numerical differentiation solutions on a more realistic domain, and upheld the conclusions reached from the convergence test. Finally, we used the direct solution to forward model a three-dimensional source with complex geometry. This involved computing a horizontal

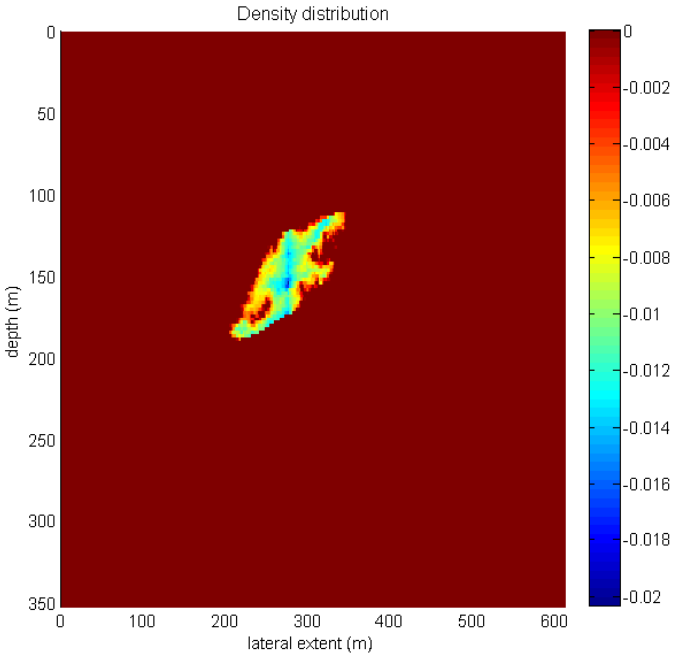

Figure 5.8: Profile of two-dimensional slice through the simulated three-dimensional Cranfield reservoir model. Density data reported in negative values with units g/cm^3; zero background density.

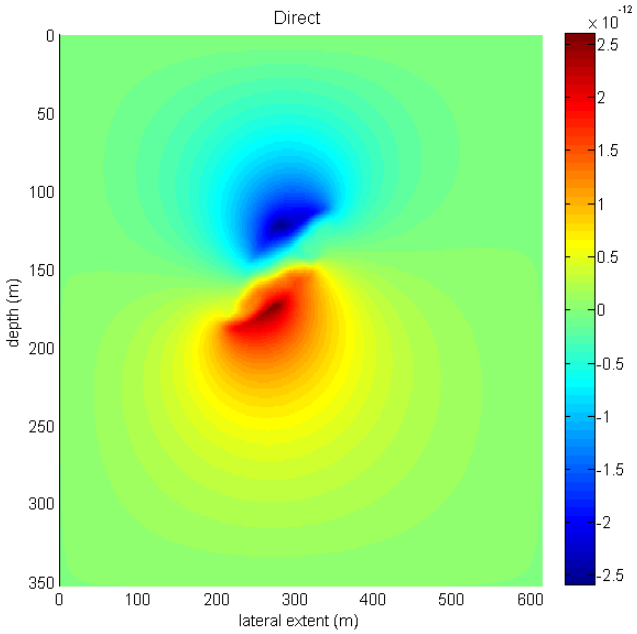

(a) g_z

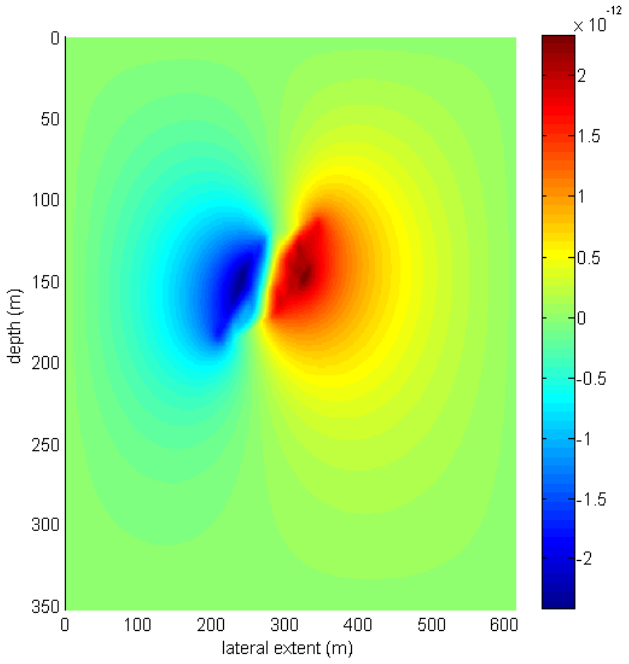

(b) g_x

Figure 5.9: Gravitational acceleration solutions produced by the Cranfield model; (a) vertical component and (b) horizontal component in x direction.

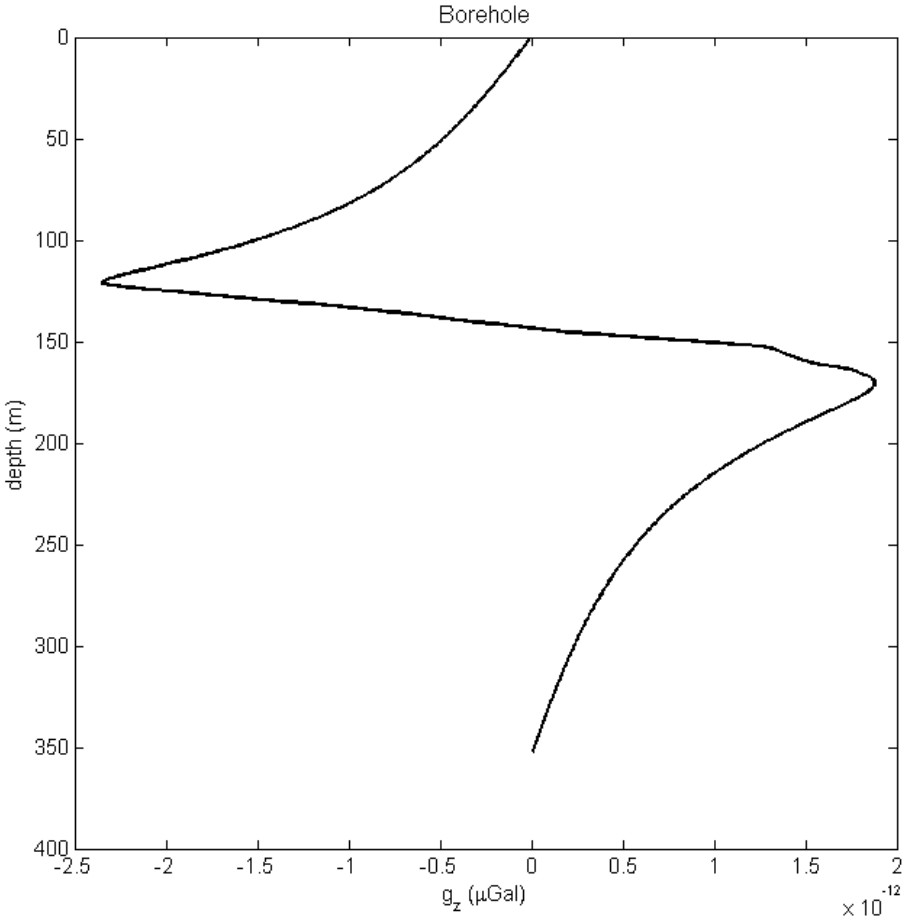

Figure 5.10: Vertical component of gravitational acceleration computed along a borehole passing through the center of the simulated full Cranfield reservoir.

component of gravitational acceleration in addition to the vertical component, and calculating the vertical component solution for a borehole passing through the source region. In the last and final chapter, we draw conclusions from these results and mention a few areas for future work.

CHAPTER 6
CONCLUSIONS

A numerical solution of Poisson's equation for gravitational acceleration was presented, demonstrating that components of gravitational acceleration can be calculated directly from a given density distribution. Finite-difference and finite-volume schemes were implemented in computing these direct solutions, and subsequently tested against benchmark solutions for simple synthetic problems. Following this verification, a direct solution of the vertical component of gravitational acceleration was presented for a realistic reservoir model.

6.1 Synthetic examples

The direct solution approach calculates the scalar components of gravitational acceleration directly from Poisson's equation; this method is numerically validated through implementation of synthetic test problems in Section 5.1. Comparisons between our new direct solution and the traditional integral and numerical differentiation solutions were made. The results demonstrate the capacity of the direct solution in resolving simple source bodies, particularly when computing gravity values for borehole simulations.

Convergence testing of the direct finite-difference and direct finite-volume solutions shows that the finite-volume formulation is able to compute solutions using a significantly smaller grid than the finite-difference formulation. This feature was initially established on a small test domain, and later demonstrated through synthetic problems with more realistic domains. Comparisons were also made between the direct and integral solutions. For simple source geometries, the integral solution produces highly accurate results that we take to be the exact solution. For a three-dimensional borehole scenario, we find that the direct solution produces comparable results to the benchmark integral solution. Through this comparison, we also find that the finite-difference and finite-volume schemes yield equivalent direct solutions.

We also find that the direct finite-difference and direct finite-volume solutions match closely with the established numerical partial differential equation solution, here referred to as the numerical differentiation solution. The gravity field solutions are compared visually and the error between the direct finite-difference and numerical differentiation solutions is quantified. Again, comparison between the finite-difference and finite-volume implementations of the direct solution shows that an equivalent finite-volume result can be obtained using fewer grid points.

All of these tests were conducted using regular structured grids with uniform cells; unstructured or nonuniform grids were not considered. These types of grids are able to better model the shape of complex source geometries, and are easily accommodated by finite volume schemes. Hence, for real geophysical applications, unstructured grids may improve upon our current results. Since we have established that the finite-volume formulation of the direct solution yields accurate results under uniform grids, extending this technique to nonuniform or unstructured grids could be considered in future work.

6.2 Reservoir application

After establishing the direct solution as a suitable alternative to conventional methods using synthetic problems, this technique was applied to a realistic source distribution. For complex source bodies like the one generated for this problem, solutions in three-dimensions are most useful. Solutions of the vertical and horizontal components of gravitational acceleration were computed. The results show that the direct solution resolves the edges of the reservoir in the x and z dimensions, as well as its tilted orientation in the domain. The borehole simulation also produces the expected result, resolving the location of the top and bottom of the reservoir.

We have shown that computing the vertical component of gravitational acceleration using the direct solution resolves large-scale features of the reservoir. Adding more information to these results would lead to a more complete delineation of the reservoir. For instance, adding more boreholes throughout the region would allow for interpretation about reser-

voir features on a finer scale than the full component solution of gravitational acceleration. Furthermore, the results of the direct solution in this application should be compared to established solutions. At this time, we leave these investigations for future studies.

6.3 Horizontal component solutions

The work presented here has primarily focused on implementing solutions for the vertical component of gravitational acceleration using our new direct technique. Since g_z is the component typically studied in geophysical literature, our comparisons to traditional solutions were conducted using this component. It is important to note, however, that the governing equation for the direct solution may easily be formulated in terms of the horizontal components g_x and g_y as follows:

$$\nabla^2 g_x = -4\pi\gamma\frac{\partial\rho}{\partial x}, \quad \text{and} \quad \nabla^2 g_y = -4\pi\gamma\frac{\partial\rho}{\partial y}.$$

As the results of the Cranfield reservoir application indicate, incorporating this information into forward models of gravitational acceleration increases the capability of gravitational acceleration solutions to resolve source bodies. Since instruments that can measure the horizontal components of gravitational acceleration are on the horizon, this information will be highly relevant for the kinds of geophysical inverse problems for which these forward models are developed. As such, extending the work developed here to horizontal component solutions is an important consideration that should be studied further.

REFERENCES CITED

[1] Chris Nind. personal communication, 2012.

[2] X. Li and M. Chouteau. Three-dimensional gravity modeling in all space. *Surveys in Geophysics*, **19**:339–368, 1998.

[3] L. C. Evans. *Partial Differential Equations*. American Mathematical Society, second edition, 2010.

[4] R. J. Blakely. *Potential theory in gravity and magnetic applications*. Cambridge University Press, 1996.

[5] U. Vogt, J. Makris, B. M. O'Reilly, F. Hauser, P. W. Readman, A. W. B. Jacob, and P. M. Shannon. The Hatton Basin and continental margin: Crustal structure from wide-angle seismic and gravity data. *Journal of Geophysical Research*, **103**:12545–12566, 1998.

[6] V. J. S. Grauch, B. D. Rodriguez, and M. Deszcz-Pan. How geophysical methods have been used to understand the subsurface. In J. R. Bartolino and J. C. Cole, editors, *Ground-water resources of the middle Rio Grande basin, New Mexico*, pages 36–37. U.S. Geological Survey Circular 1222, 2002.

[7] M. N. Nabighian, M. E. Ander, V. J. S. Grauch, R. O. Hansen, T. R. LaFehr, Y. Li, W. C. Pearson, J. W. Pierce, J. D. Phillips, and M. E. Ruder. Historical development of the gravity method in exploration. *Geophysics*, **70**:63ND–89ND, 2005.

[8] R. Krahenbuhl and Y. Li. Time-lapse gravity: A numerical demonstration using robust inversion and joint interpretation of 4d surface and borehole data. *Geophysics*, **77**: G33–G43, 2012.

[9] W. Lowrie. *Fundamentals of geophysics*. Cambridge University Press, 2007.

[10] C. R. W. Mosher, C. G. Farquharson, and C. A. Hurich. Minimum-structure borehole gravity inversion. In *Presented at the Annual Meeting, Society of Exploration Geophysicists*, 2008.

[11] C. G. Farquharson and C. R. W. Mosher. Three-dimensional modelling of gravity data using finite differences. *Journal of Applied Geophysics*, **68**:417–422, 2009.

[12] H. Jahandari and C. G. Farquharson. Forward modelling of gravity data for unstructured grids using the finite-volume method. In *Presented at the Annual Meeting, Society of Exploration Geophysicists*, 2011.

[13] J. Zhang, C.-Y. Wang, Y. Shi, W.-C. Chi, D. Dreger, W. B. Cheng, and Y. H. Yuan. Three-dimensional crustal structure of central Taiwan from gravity inversion with a parallel genetic algorithm. volume 69, pages 917–924, 2004.

[14] A. Dey and H. F. Morrison. Resistivity modelling for arbitrarily shaped two-dimensional structures. *Geophysical Prospecting*, **27**:106–136, 1979.

[15] M. Andy Kass. personal communication, 2012.

[16] R. Eymard, T. Gallouët, and R. Herbin. Finite volume methods. In P. G. Ciarlet and J. L. Lions, editors, *Handbook of Numerical Analysis*, pages 713–1020. North-Holland, 2003.

[17] A. Jeffrey. *Applied Partial Differential Equations: An Introduction.* Academic Press, 2002.